Reunderstanding Aqueous Zn Electrochemistry from Interfacial Specific Adsorption of Solvation Structures

Hang Yang[a], Duo Chen[*,b], Ruizheng Zhao[c], Gaoyang Li[c], Hao Xu[a], Li Li[a], Xin Liu[d], Guangshe Li[a], Dongliang Chao[c], Wei Han[*,a]

[a]College of Physics, College of Chemistry, State Key Laboratory of Inorganic Synthesis and Preparative Chemistry, International Center of Future Science, Jilin University, Changchun 130012, P.R. China
[b]Jiangsu Key Laboratory of Electrochemical Energy Storage Technologies, College of Materials Science and Technology, Nanjing University of Aeronautics and Astronautics, Nanjing 210016, China
[c]Laboratory of Advanced Materials, Shanghai Key Laboratory of Molecular Catalysis and Innovative Materials, and School of Chemistry and Materials, Fudan University, Shanghai 200433, P. R. China
[d]Key Laboratory of Engineering Dielectric and Applications (Ministry of Education), School of Electrical and Electronic Engineering, Harbin University of Science and Technology, Harbin 150080, P. R. China

Corresponding E-mail：E-mail: whan@jlu.edu.cn (W. H.), chenduo@nuaa.edu.cn (D. C.)
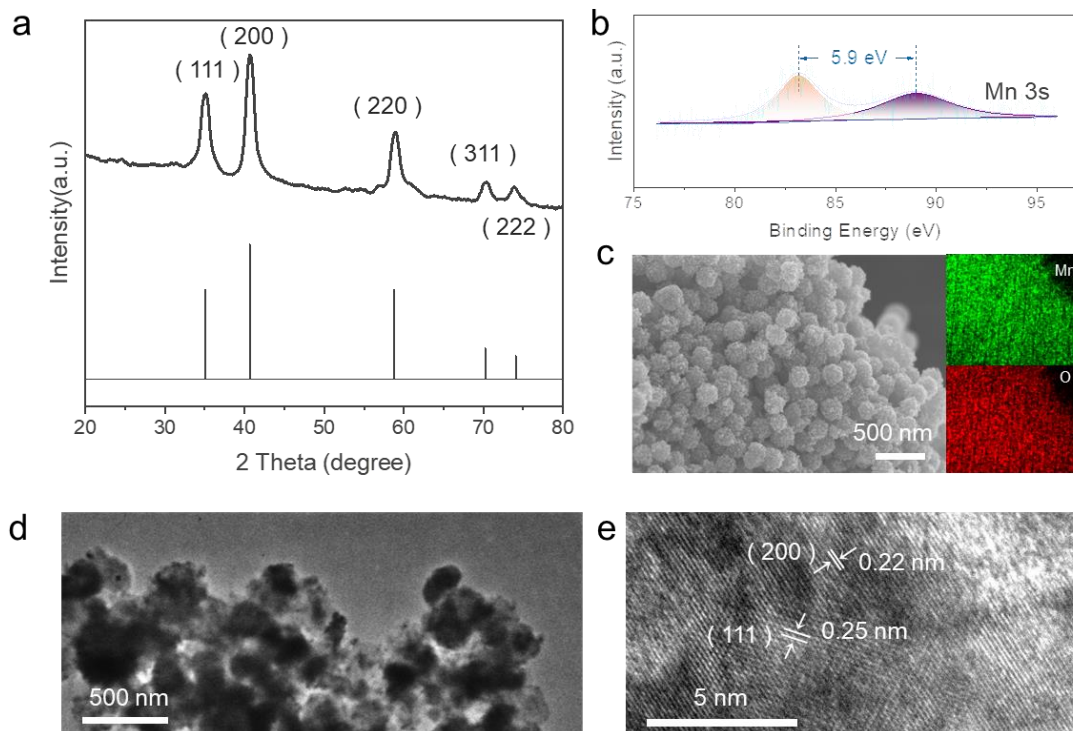
Fig. S1. The characterization of MnO nanoparticles. (a) XRD patterns; (b) XPS spectra of Mn 3s; (c) SEM image (EDX element mapping, inset); (b) TEM image and (e) HRTEM image.

Fig. S1a reveals the X-ray diffraction (XRD) patterns of obtained MnO. The characteristic diffraction peaks are well indexed to pure MnO (JCPDS 97-006-8916) with a face-centered cubic phase. The chemical compositions by X-ray photoelectron spectroscopy (XPS) (Fig. S1b), exhibit a spin-energy separation of 5.9 eV for the Mn 3s doublet, indicating the Mn has a charge state of ∼2. The scanning electron microscopy (SEM) (Fig. S1c) and transmission electron microscopy images (TEM, Fig. S1d) of the MnO show that they possess a nanoparticle morphology. The energy-dispersive X-ray spectroscopy (EDX) results present the uniform spatial distribution of the involved elements. Furthermore, the typical interplanar spacing of 0.25 nm and 0.22 nm in high-resolution TEM (HRTEM, Fig. S1e) corresponds to the (111) and (200) planes of MnO. Therefore, the successful synthesis of MnO nanoparticles was demonstrated.
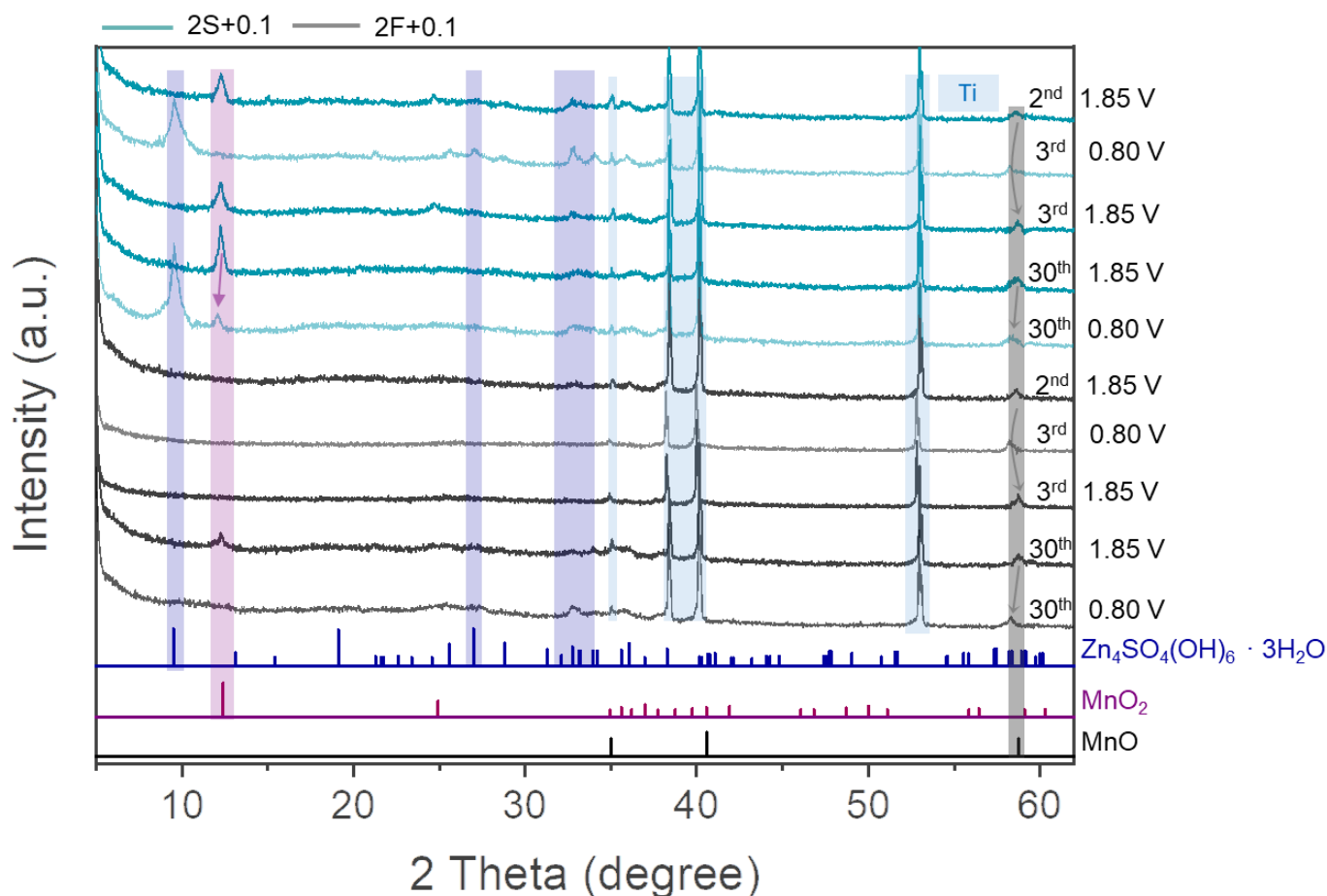
Fig. S2. *Ex situ* XRD patterns of the MnO-based cathode with different electrolytes during the charge/discharge process. JCPDS No.: MnO 97-006-0691, MnO_2 97-006-8916, $Zn_4SO_4(OH)_6 \cdot 3H_2O$ 97-006-1115

The cycled MnO electrodes were collected for XRD characterization in both electrolytes at the various stages (Fig. S2). The diffraction peaks of MnO are well preserved with the reversible shift of the peak at ~58.7° due to the insertion of Zn^{2+}.

HRTEM images (Fig. S3) confirm the expansion to ~0.28 nm of (111) crystal plane for MnO cathode at the discharged state in both electrolytes, compared with the pristine MnO cathode (0.25 nm), indicating the insertion of Zn^{2+}.[1, 2] A high content of Zn element is detected at the deep discharge state of 0.8 V, indicating a mass of Zn^{2+} insert into the cathode. The uniform distribution and atom ratios of Zn further verify the (de)intercalation behavior of Zn^{2+} supported by EDS analysis (Fig. S4).

Intriguingly, the deposition/dissolution behavior of δ−MnO_2 (diffraction peak at ~12.26°) can be clearly observed in 2S+0.1 electrolyte (Fig. S2). However, involved diffraction peaks caused by deposition cannot be gathered in the cell using the pure 2 M $ZnSO_4$ electrolyte (Fig. S5), determining that the δ−phase MnO_2 evolves from the electrolyte containing Mn^{2+}.[3] The transmission electron microscopy (TEM, Fig. S6a) detects the co−existence of nanoflowers and nanoparticles in the 2S+0.1 electrolyte. The typical interplanar spacing (001) of 0.72 nm

3

for δ−MnO$_2$ is detected by high−resolution TEM (HRTEM, Fig. S6b), which testifies the nanoflowers as δ−MnO$_2$. Similar electrodeposition behaviors were distinctly obtained in the 2F+0.1 electrolyte only after long cycling *via* XRD characterization (Fig. S2), indicating weak deposition behavior. SEM images (Fig. S4) reveal that the morphology of the deposited sediment covering the MnO nanoparticles with a morphology of nanoflower−like (marked with cyan) in 2S+0.1 electrolyte at 1.85 V, which is significantly more than that in the 2F+0.1 electrolyte. The apparent deposition of manganese will provide additional capacity for 2S+0.1 electrolyte.[4]
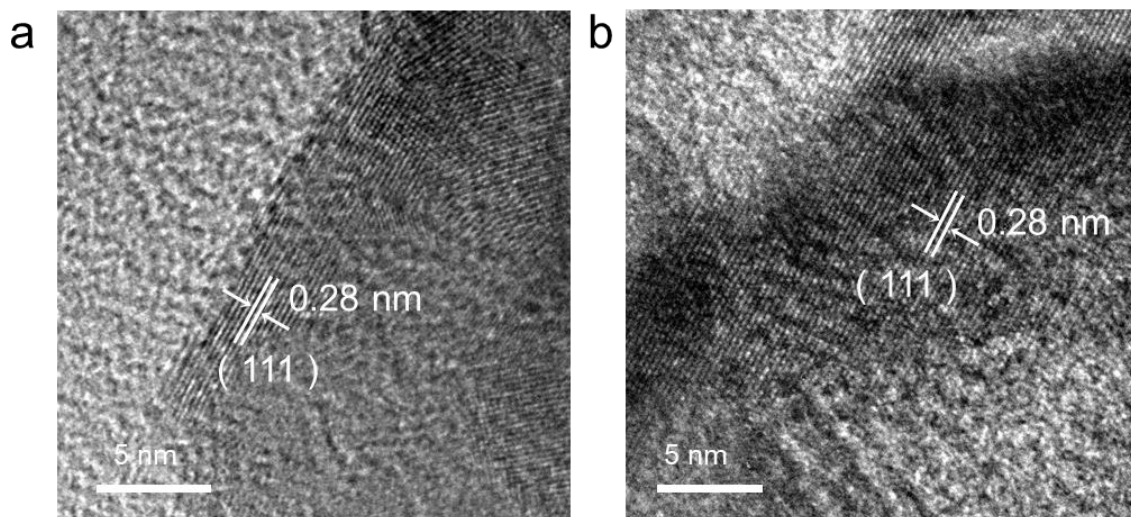
Fig. S3. HRTEM images of (111) crystal planes for MnO-based cathode in fully discharged states in the (a) 2S+0.1 electrolyte, (b) 2F+0.1 electrolyte, showing that ion intercalation causes lattice spacing expansion.
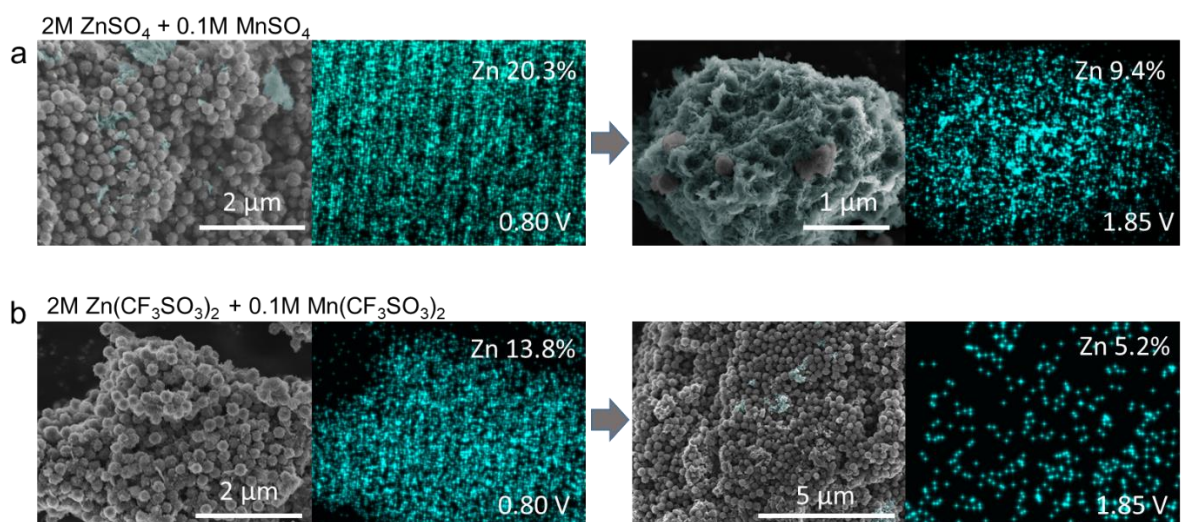
Fig. S4. The content of Zn element determined by SEM-EDX at charged/discharged stage: (a) in 2S+0.1 electrolyte (The cyan shadows are undissolved MnO_2); (b) in 2F+0.1 electrolyte.
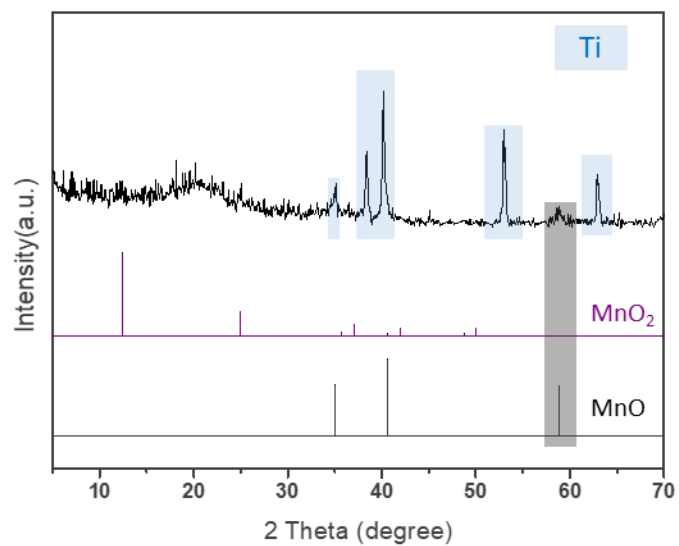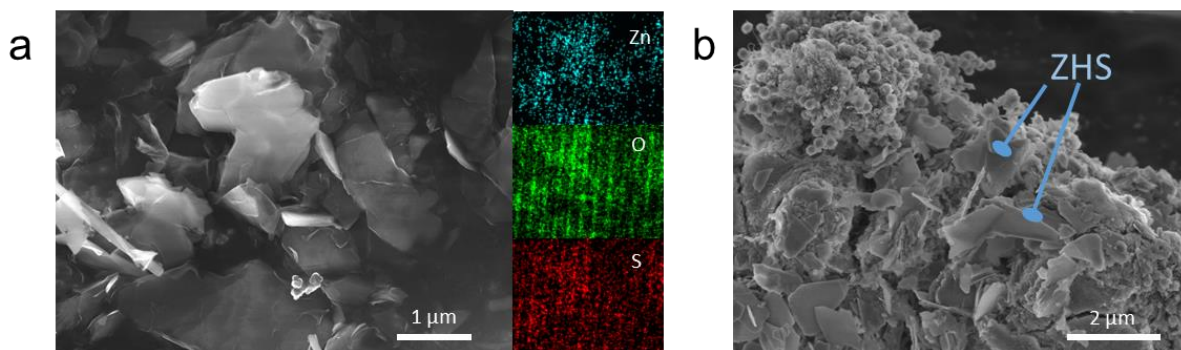
**Fig. S5.** XRD patterns of the MnO-based cathode in 2M ZnSO$_4$ electrolyte
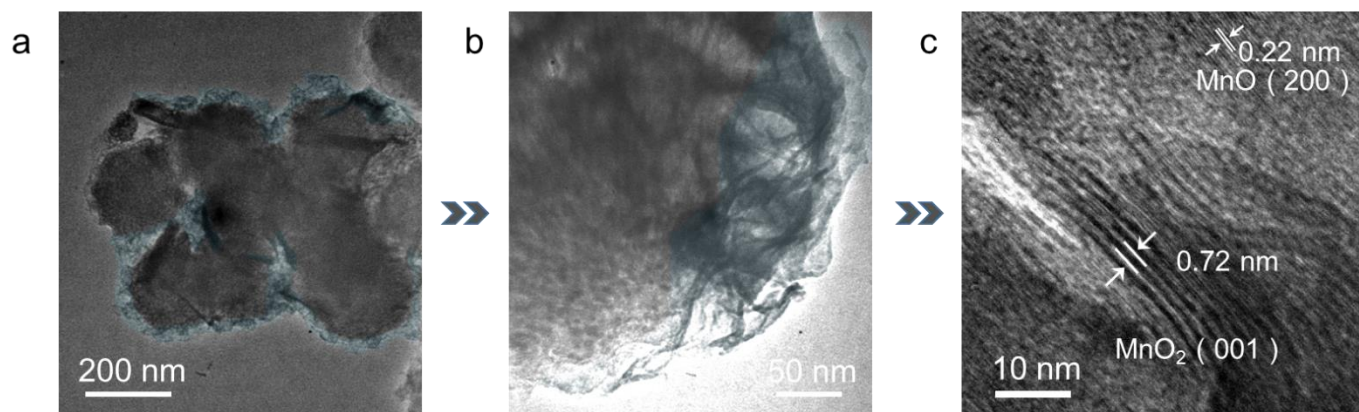
Fig. S6. TEM and HRTEM images of MnO-based cathode in the 2S+0.1 electrolyte. MnO_2 nanoflowers is marked by cyan.

Fig. S7. The SEM/EDX images of cathode using 2S+0.1 electrolyte.

The diffraction peak at 9.7° corresponding to basic zinc sulfate ($Zn_4SO_4(OH)_6 \cdot 3H_2O$, noted as ZHS, Fig. S2) appears opposite to that of δ−phase MnO_2, which might be due to the increase of the local pH caused by appendant consumption for (de)intercalation of H^+ into MnO host in addition to dissolved δ−phase MnO_2 at the discharged process.[2] SEM image (Fig. S7) presents that only ZHS precipitates is close to the MnO nanoparticles, while MnO_2 disappears, indicating that the (de)intercalation of H^+ is MnO in the electrolyte containing SO_4^{2-}. The process of ZHS precipitation triggers by OH^- accumulation after the H^+ insertion could be defined as follow:

$$4Zn^{2+} + 6OH^- + SO_4^{2-} + 3H_2O \leftrightarrow Zn_4SO_4(OH)_6 \cdot 3H_2O \qquad (4)$$
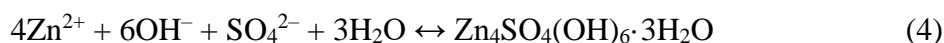
In detail, the involved H^+ in the process of deposition ($Mn^{2+} \rightarrow MnO_2$) and dissolution ($MnO_2 \rightarrow Mn^{2+}$) should be equal, so ZHS will only be generated in the presence of other electrochemical behaviors that consume H^+ during discharge process. Furthermore, ZHS precipitation occurs on the surface of the electrode material only when the OH^- are accumulated triggered by insertion of H^+ into the host.[5] Fig. S7a shows a selected independent nano-sheet for the analysis of element composition in 2S+0.1 electrolyte, indicating that it is ZHS. The SEM image (Fig. S7b) in the discharged state proves that the MnO_2 dissolves and nano-sheet ZHS precipitation generates sticking to electrode surface of MnO cathode caused by the excessive consumption of H^+. This ZHS precipitation mechanism is very similar to that in widely reported high-valent manganese oxide electrodes.[6] It is worth noting that in the electrolyte containing $CF_3SO_3^-$, the precipitation reaction is so difficult to occur that it cannot be detected by XRD patterns even though the insertion of H^+, which might attribute to binding energy between Zn^{2+} and $CF_3SO_3^-$ is weaker than that of SO_4^{2-} (Fig. S8). In order to affirm the intercalation behavior of H^+ in the $CF_3SO_3^-$ electrolyte, the MnO cathode is assembled into a coin cell in 2 M $Zn(CF_3SO_3)_2$ + 0.1 M $MnSO_4$ electrolyte. The ZHS precipitation is clearly detected by XRD patterns and SEM image (Fig. S9) at the

discharge state, indicating the H^+ intercalation in the electrolyte containing many $CF_3SO_3^-$. It also hints that this trace SO_4^{2-} tip could be served as an intelligent agent to reveal the masked H^+ intercalation behavior in potential aqueous batteries (ABs) system.
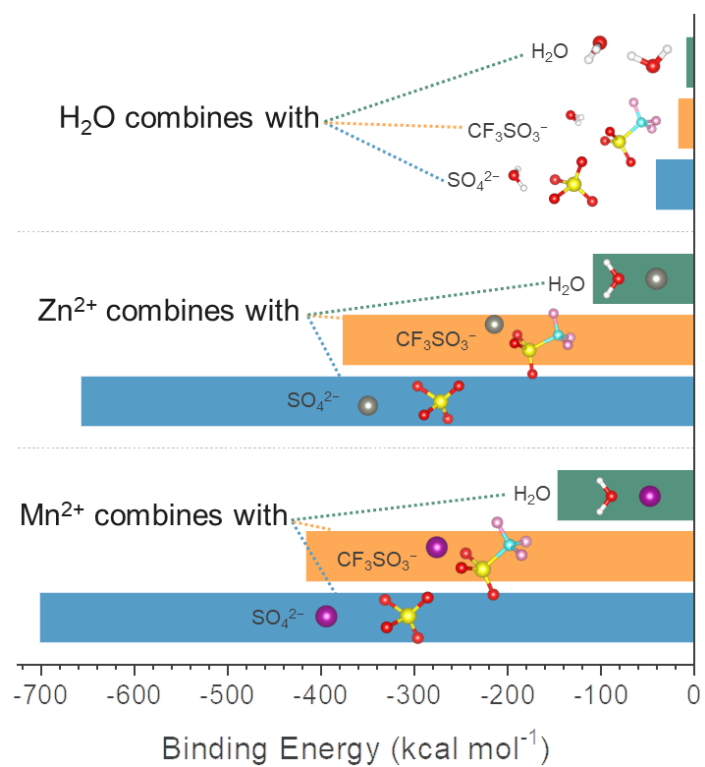
Fig. S8. The configurations and binding energies of $Zn^{2+}/Mn^{2+}/ H_2O$—$H_2O/ CF_3SO_3^-/ SO_4^{2-}$ conducted by DFT calculation.
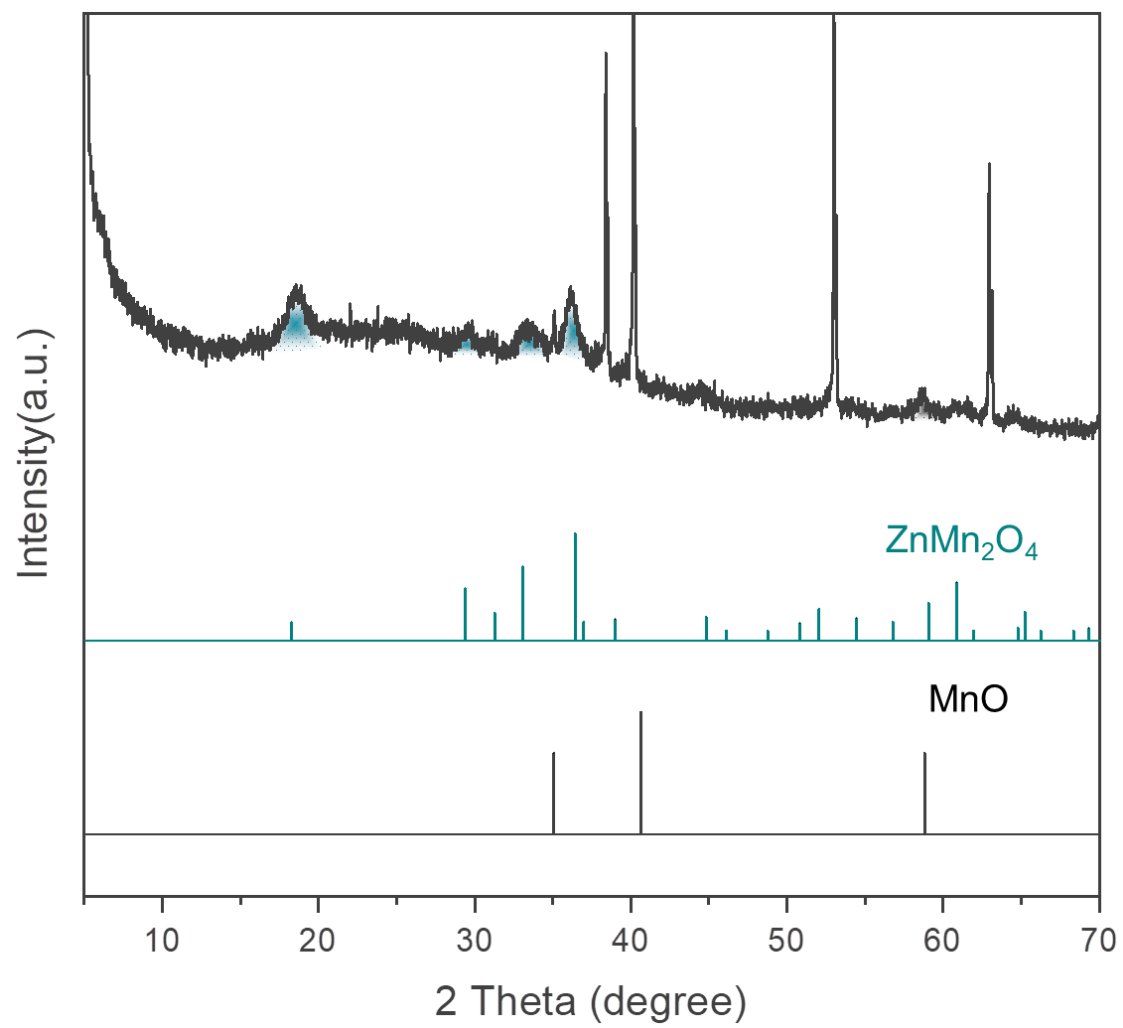
11
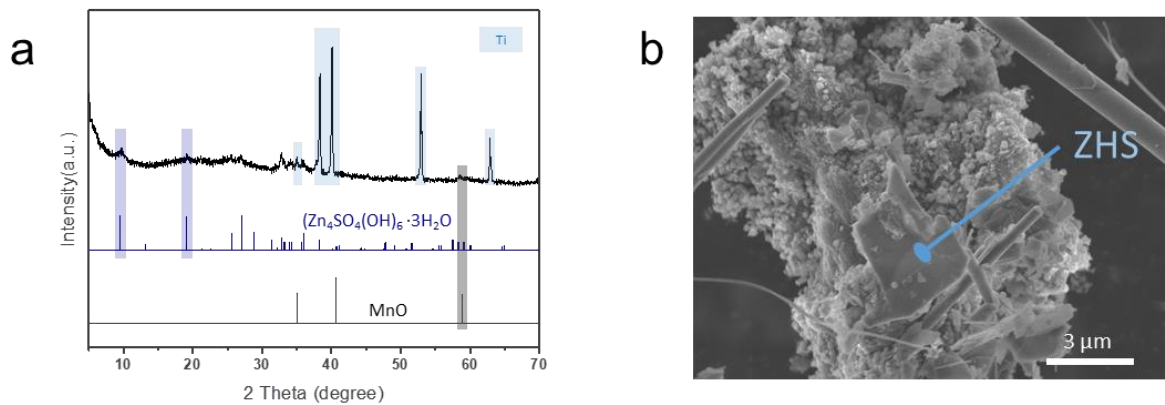
Fig. S9. The XRD patterns and SEM image of cathode using 2 M $Zn(CF_3SO_3)_2$ + 0.1 M $MnSO_4$ electrolyte.
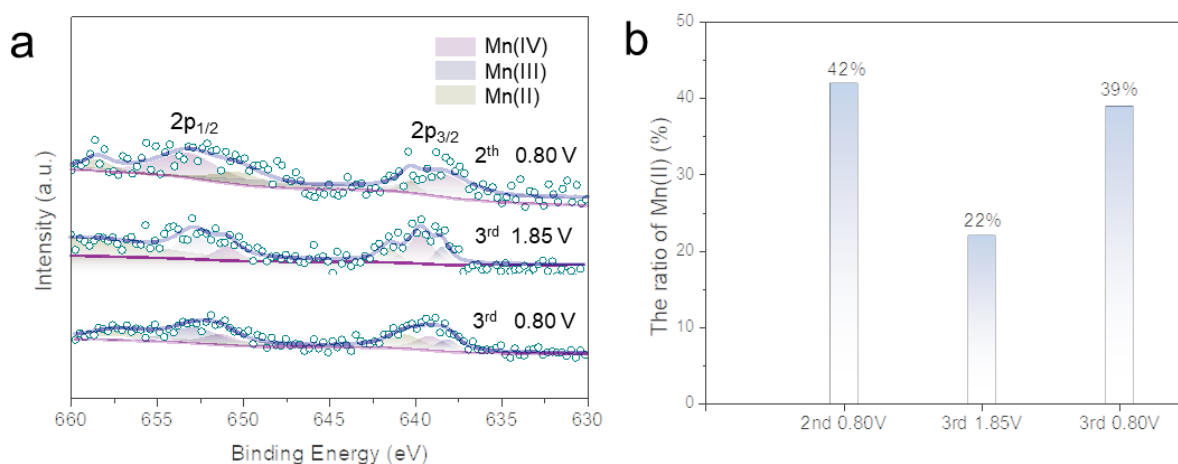
Fig. S10. The XPS spectra of (e) Mn 2p for the MnO-based cathode obtained from the cells with 2M $ZnSO_4$ electrolyte at different states. (b) The reversible change in the ratio of Mn (II) at different states by XPS spectra. Note: No Mn^{2+} additive was added to prevent the interference of high manganese oxide from electrolyte oxygenation.

According to previous reports, MnO is activated to MnO_x during charging process, which is used to store Zn^{2+}/H^+.[1, 7, 8] The XPS results (Fig. S10) in different states also confirmed the conclusion that the reversible transformation of divalent manganese indicated the reversible redox reaction of Mn in the electrochemical process.[9, 10] Therefore, MnO is first electrochemically oxidized to MnO_X, and then the subsequent the charge/discharge mechanism can be described as:

$MnO_x + yZn^{2+} + 2ye^- \leftrightarrow Zn_yMnO_x$

$MnO_x + zH^+ + ze^- \leftrightarrow H_zMnO_x$

$4Zn^{2+} + 6OH^- + SO_4^{2-} + 3 H_2O \leftrightarrow Zn_4SO_4(OH)_6 \cdot 3H_2O$

$Mn^{2+} + 2H_2O - 2e^- \rightarrow MnO_2 + 4H^+$
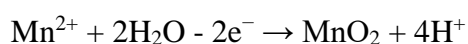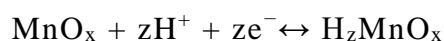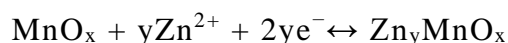
Fig. S11. *Ex situ* XRD patterns of the MnO cathode with 2S+0.1 electrolyte at 60th at 1.85 V for long-time cycle.

14
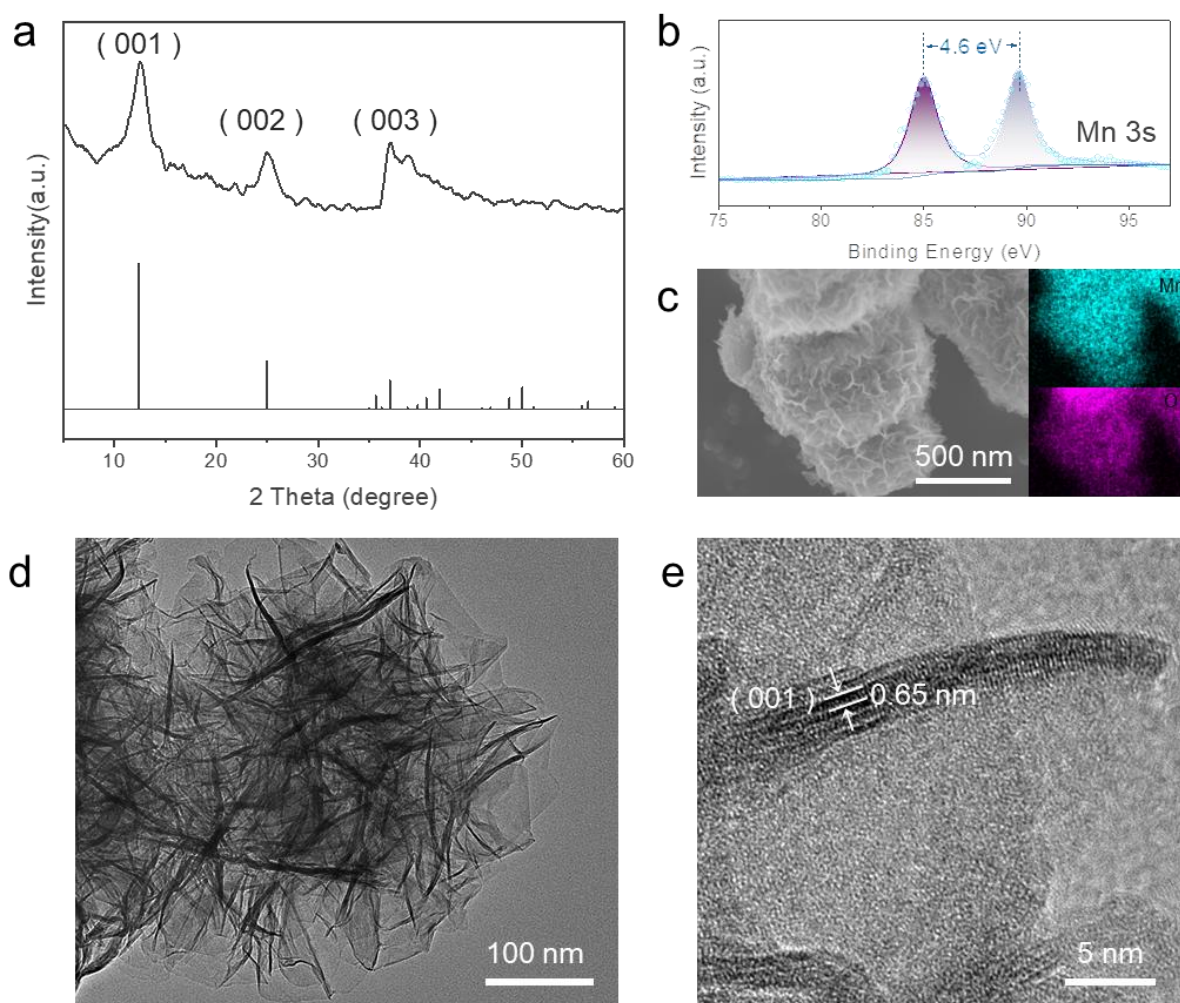
Fig. S12. The characterization of MnO$_2$ nanoflower. (a) XRD patterns; (b) XPS spectra of Mn 3s; (c) SEM (EDX element mapping, inset); (d) TEM image and (e) HRTEM image.

Fig. S12a shows the XRD pattern of obtained MnO$_2$. And the characteristic diffraction peaks are well assigned to pure δ-phase MnO$_2$ (JCPDS 97-006-8916) with a layered framework. XPS results (Fig. S12b) suggest that the Mn has a charge state of ∼4. The SEM image (Fig. S12c) and TEM image (Fig. S12d) exhibit the nanoflower structure of the obtained MnO$_2$. Meanwhile, the typical interplanar spacing of (001) plane of MnO$_2$ in the HRTEM image (Fig. S12e) was observed. Therefore, the successful synthesis of MnO$_2$ nanoflower was demonstrated.
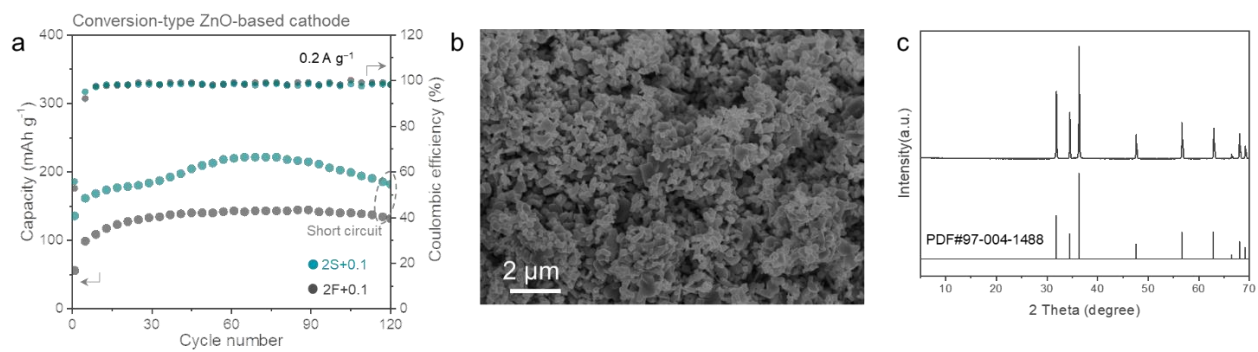
Fig. S13. (a) The electrochemical performance in different electrolyte, (b) SEM image for commercial ZnO, and (c) XRD patterns.
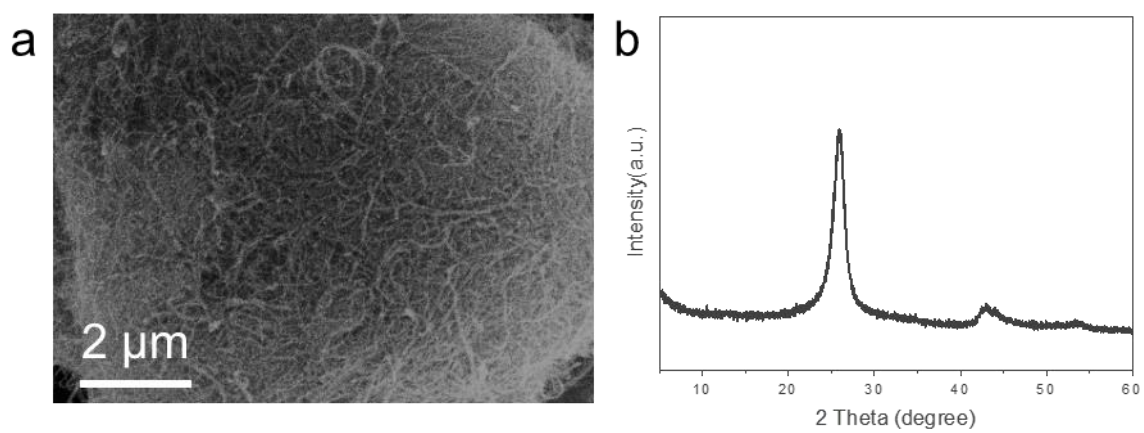
**Fig. S14.** The XRD partterns and SEM image for commercial carbon nanotubes.
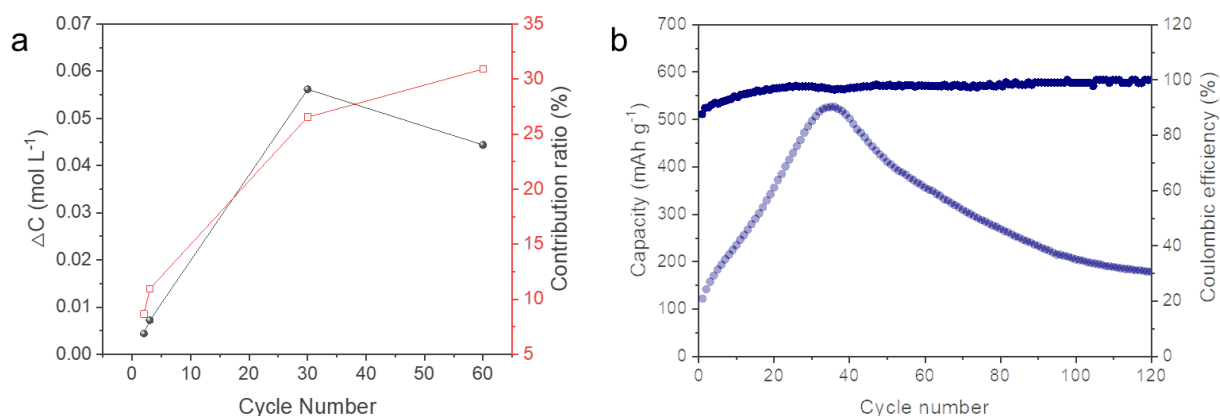
Fig. S15. (a) The concentration changes and contribution ratio of the Mn^{2+} in the 2S+0.1 electrolyte with the initial pH of 3.7 adjusted by H_2SO_4. (b) Electrochemical performance of Zn-MnO full cells in 2S+0.1 electrolyte with the initial pH of 3.7.

To unravel the concern on whether the unusual Mn^{2+} deposition behavior is induced by the pH of the electrolyte, the control cell assembled in 2S+0.1 electrolyte with the initial pH of 3.7 (the pH of 2F+0.1 electrolyte is ~3.8). Although there is a certain decrease in CCr (Fig. S15a), the overall surge trend indicates a negligible effect of lowering pH in suppressing Mn^{2+} deposition. The fluctuation of the electrochemical curve in the 2S+0.1 electrolyte at pH=3.7 is like that of original 2S+0.1 electrolyte (Fig. S15b), which is consistent with previous analysis such as ICP−OES (Fig. S15a).
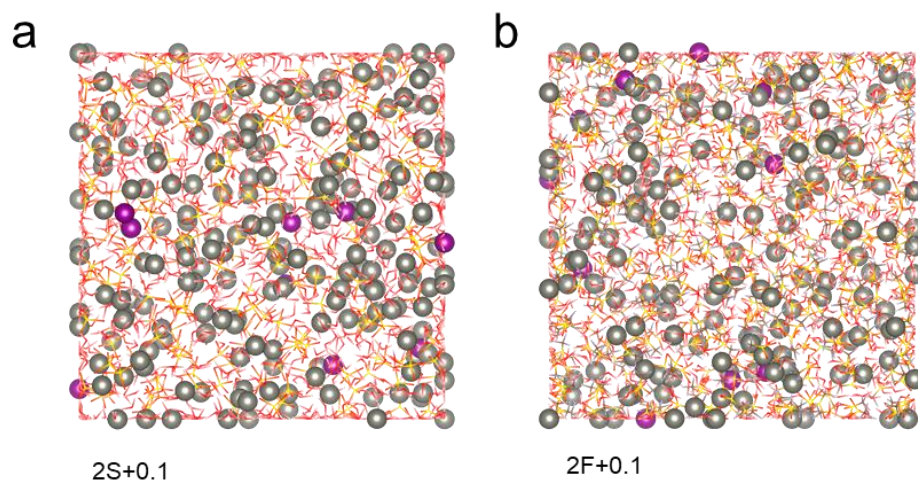
Fig. S16. (a-b) Snapshots of the equilibrated MD simulation box for the different electrolytes.
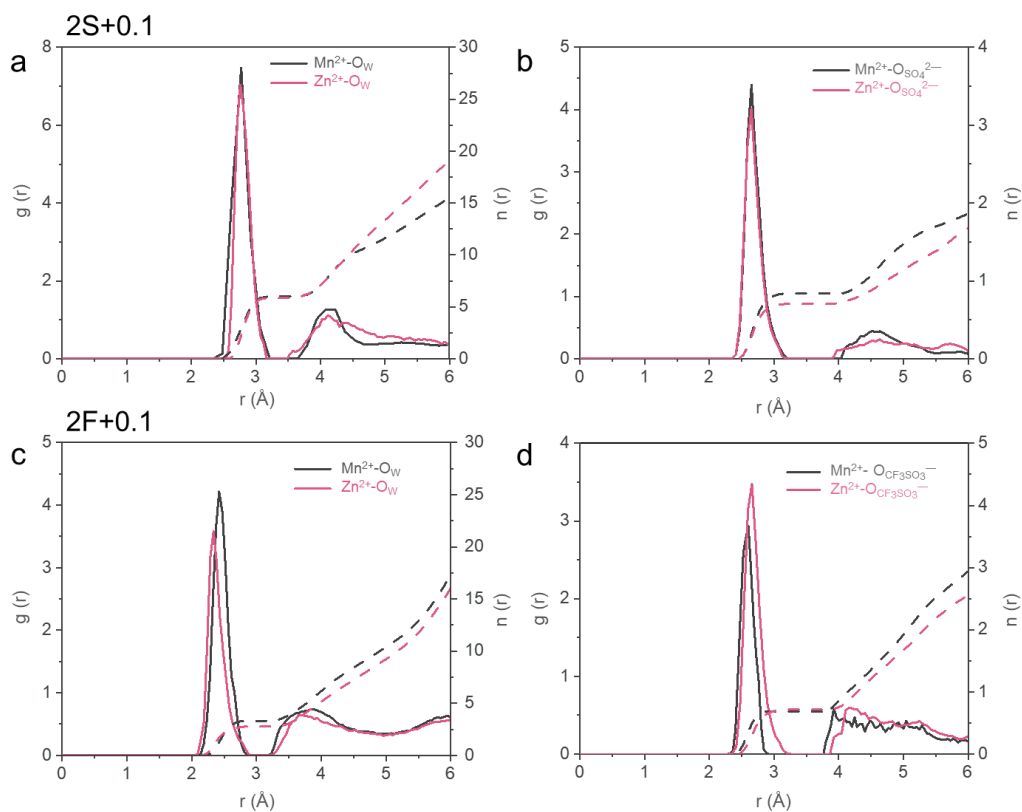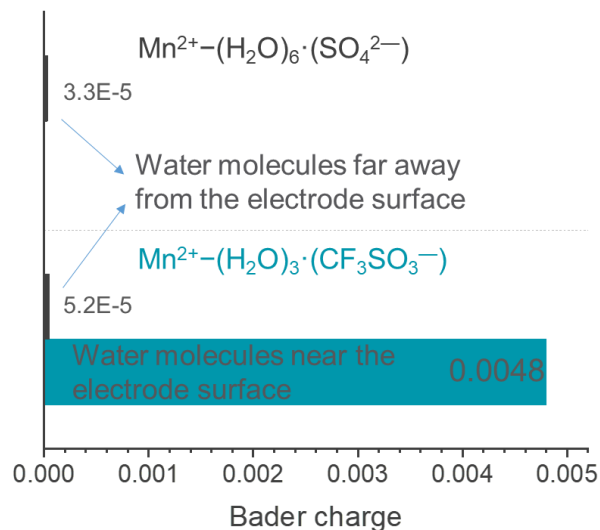
Fig. S17. The cation solvation structures in 2S+0.1 and 2F+0.1 electrolytes are expressed based on the RDFs and coordination number analyses, respectively: (a) RDFs for Zn^{2+}/Mn^{2+}-O (H_2O) and (b) Zn^{2+}/Mn^{2+}-O (SO_4^{2-}) in 2S+0.1 electrolyte; (c) RDFs for Zn^{2+}/Mn^{2+}-O (H_2O) and (e) Zn^{2+}/Mn^{2+}-O ($CF_3SO_3^-$) in 2F+0.1 electrolyte.
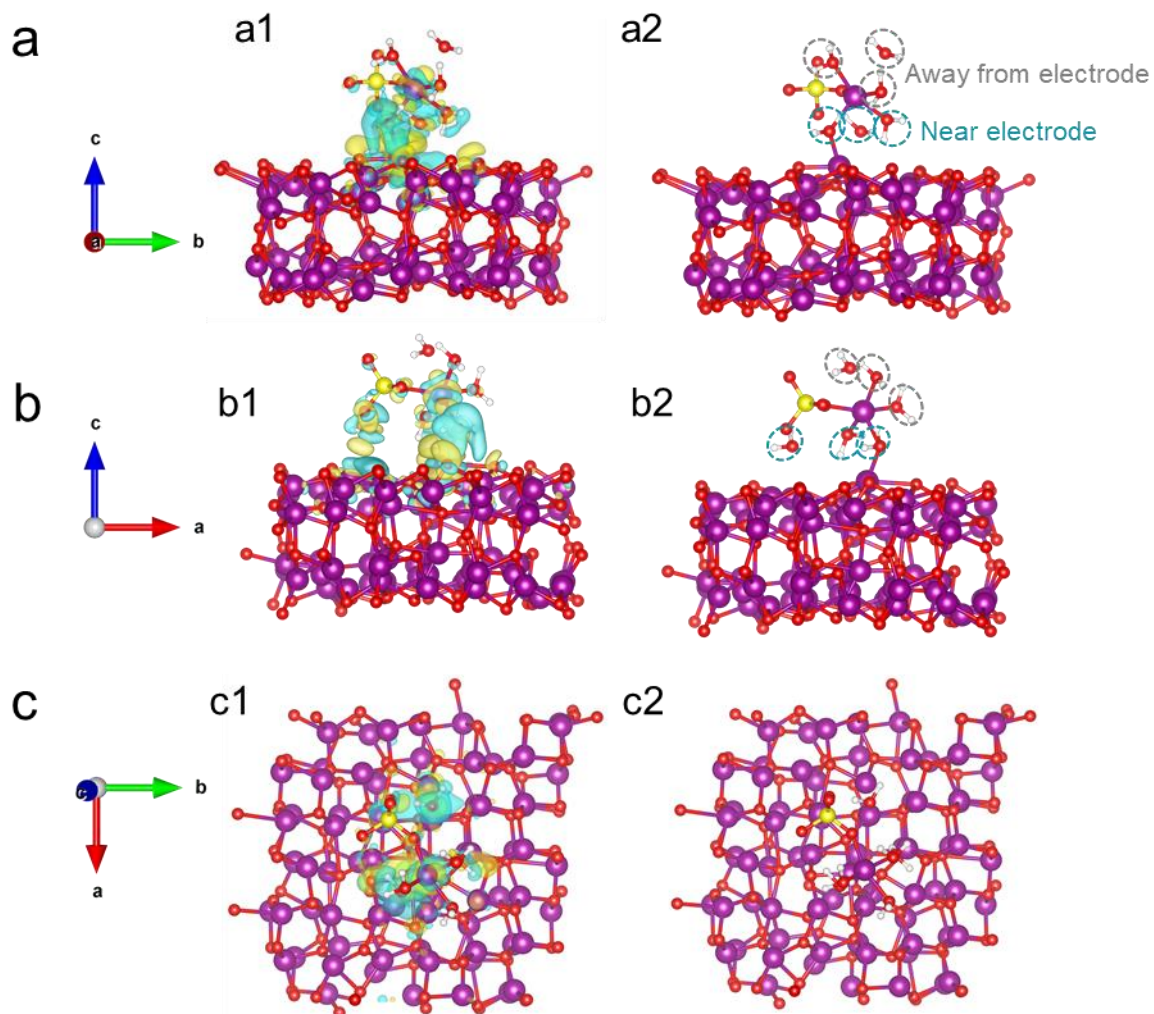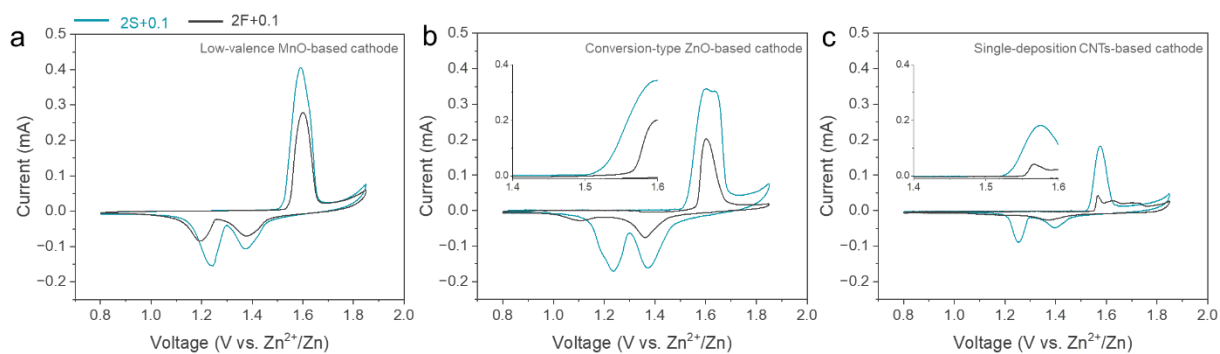
Fig. S18. (a1-c1) The charge density difference for demonstrating interfacial specific adsorption model of cathode for $Mn^{2+}-(H_2O)_6\cdot(SO_4^{2-})$. (Cyan: charge depletion; yellow: charge accumulation; isovalue=0.001 e Å^{-3}). (a2-c2) the isosurface charge density is removed.
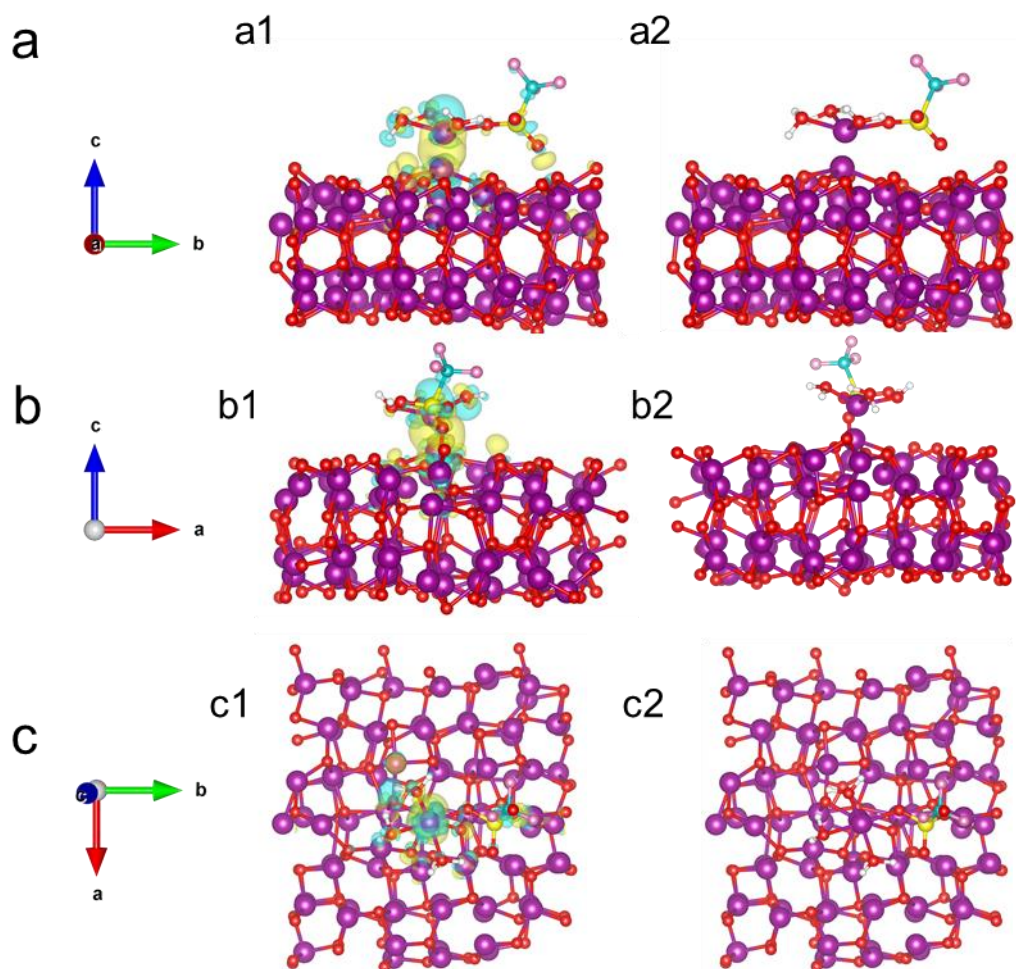
Fig. S19. (a1-c1) The charge density difference for demonstrating interfacial specific adsorption model of cathode for $Mn^{2+}-(H_2O)_3\cdot(CF_3SO_3^-)$. (Cyan: charge depletion; yellow: charge accumulation; isovalue=0.001 e Å^{-3}). (a2-c2) retain the region of charge accumulation. (a3-c3) The isosurface charge density is removed.

$Mn^{2+}-(H_2O)_6\cdot(SO_4{}^{2-})$

3.3E-5

Water molecules far away from the electrode surface

$Mn^{2+}-(H_2O)_3\cdot(CF_3SO_3{}^-)$

5.2E-5

Water molecules near the electrode surface

0.0048

0.000 0.001 0.002 0.003 0.004 0.005

Bader charge

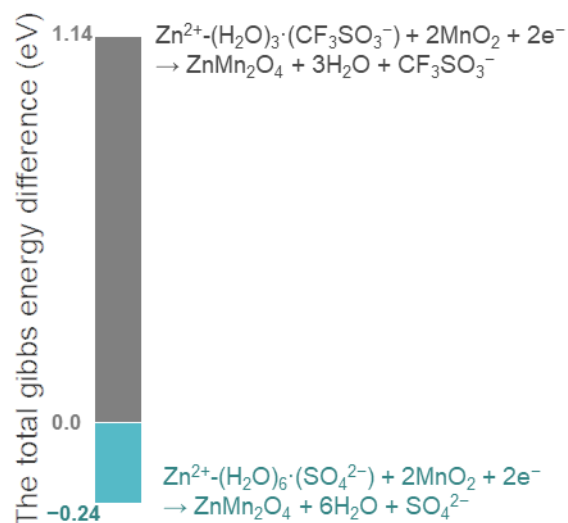**Fig. S20.** Bader charge of different position of H_2O marked in Fig. S18 and Fig. S19.

Fig. S21. The typical CV curves for the (a) MnO-based cathode/Zn cell, (b) ZnO-based cathode/Zn cell, and (c) CNTs-based cathode/Zn cell using different electrolytes at the scan rate of 0.1 mV s^{-1}
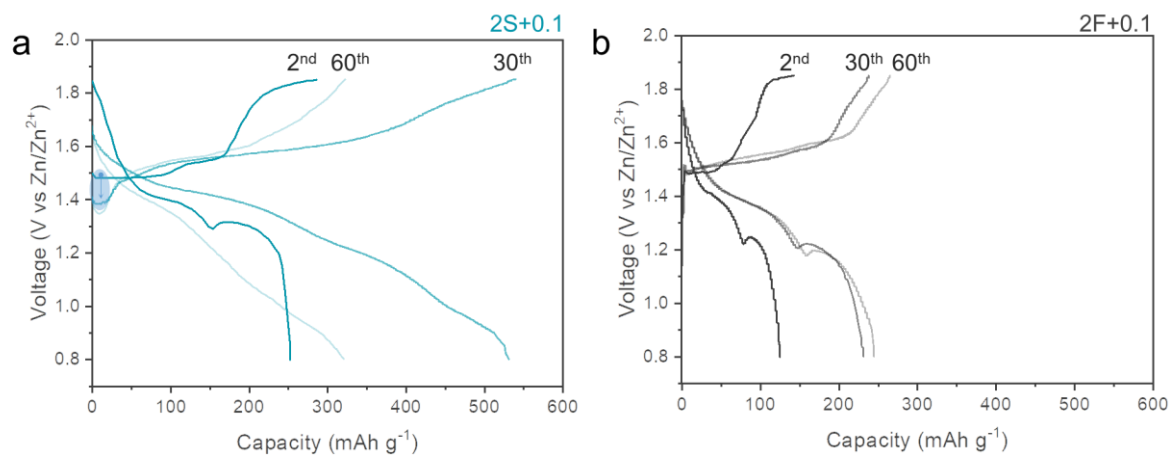
**Fig. S22.** Galvanostatic charge-discharge profiles of MnO-based cathode in the different electrolytes.

The total gibbs energy difference (eV)

1.14 — Zn^{2+}-$(H_2O)_3$·$(CF_3SO_3^-)$ + $2MnO_2$ + $2e^-$
→ $ZnMn_2O_4$ + $3H_2O$ + $CF_3SO_3^-$

0.0

Zn^{2+}-$(H_2O)_6$·(SO_4^{2-}) + $2MnO_2$ + $2e^-$
→ $ZnMn_2O_4$ + $6H_2O$ + SO_4^{2-}

−0.24

Fig. S23. The total Gibbs energy difference of the transition from layered MnO_2 to spinel $ZnMn_2O_4$ influenced by solvation structure.

2S+0.1
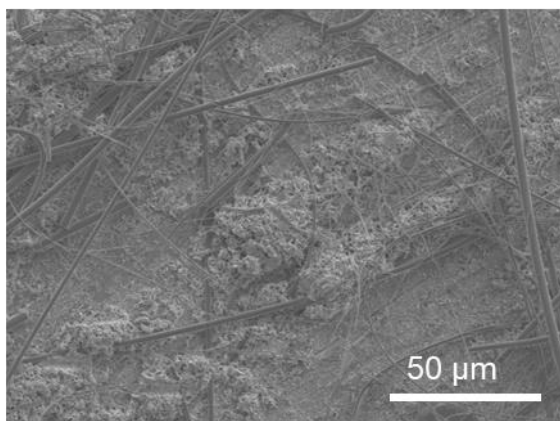
2F+0.1
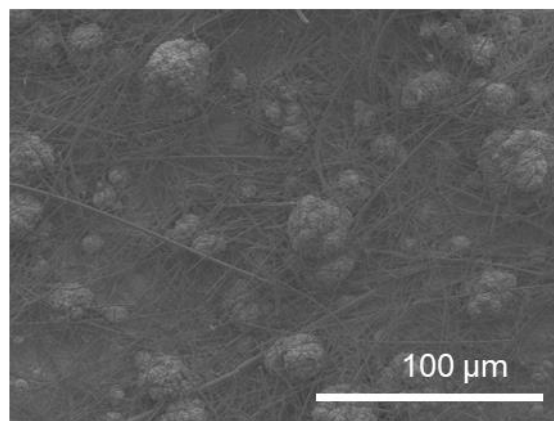

**Fig. S24.** SEM images of Zn anode at a current density of 5 mA cm^{-2} and capacity of 2.5 mAh cm^{-2} under the different electrolytes.
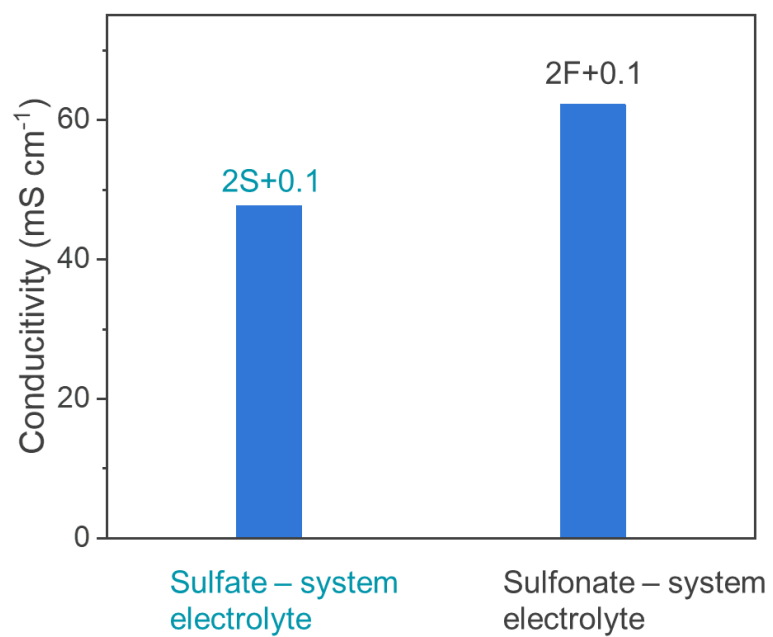
Fig. S25. Ionic conductivity of different electrolytes.
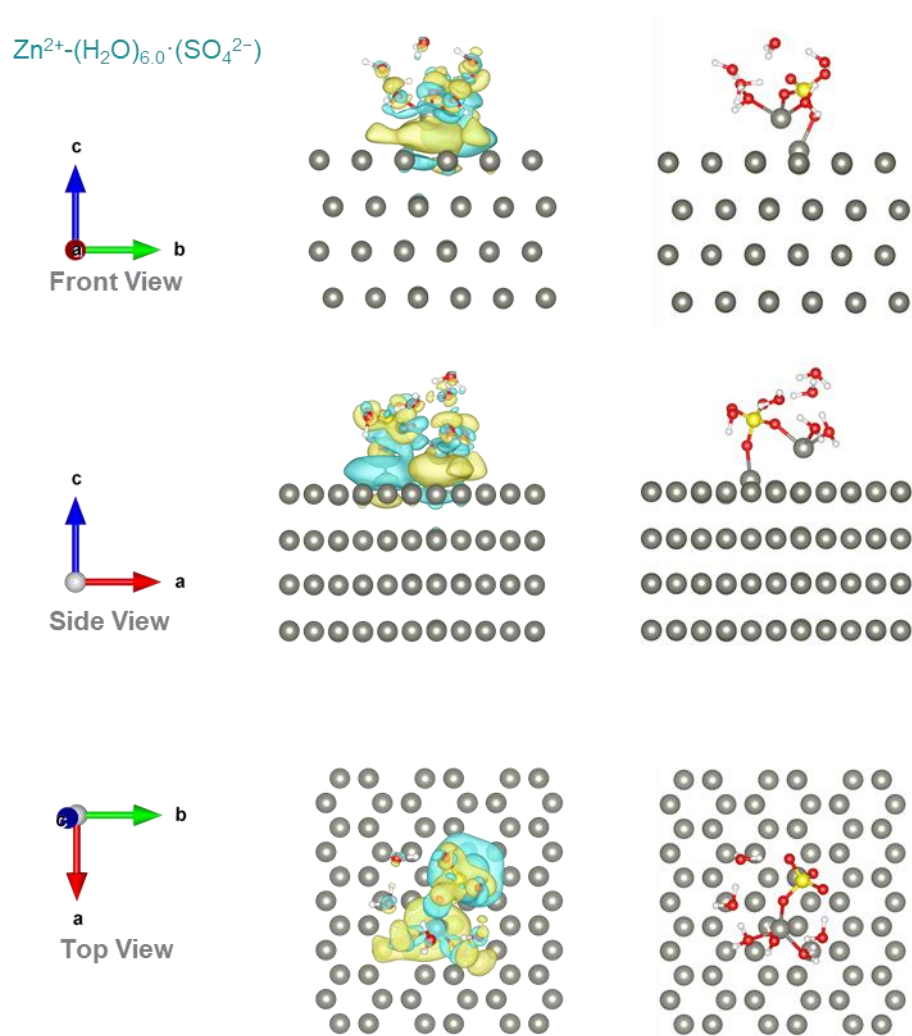
**Fig. S26.** The charge density difference for demonstrating interfacial specific adsorption model of anode for $Zn^{2+}-(H_2O)_6 \cdot (SO_4^{2-})$. (Cyan: charge depletion; yellow: charge accumulation; isovalue=0.001 e Å^{-3}). The isosurface charge density on the right is removed.
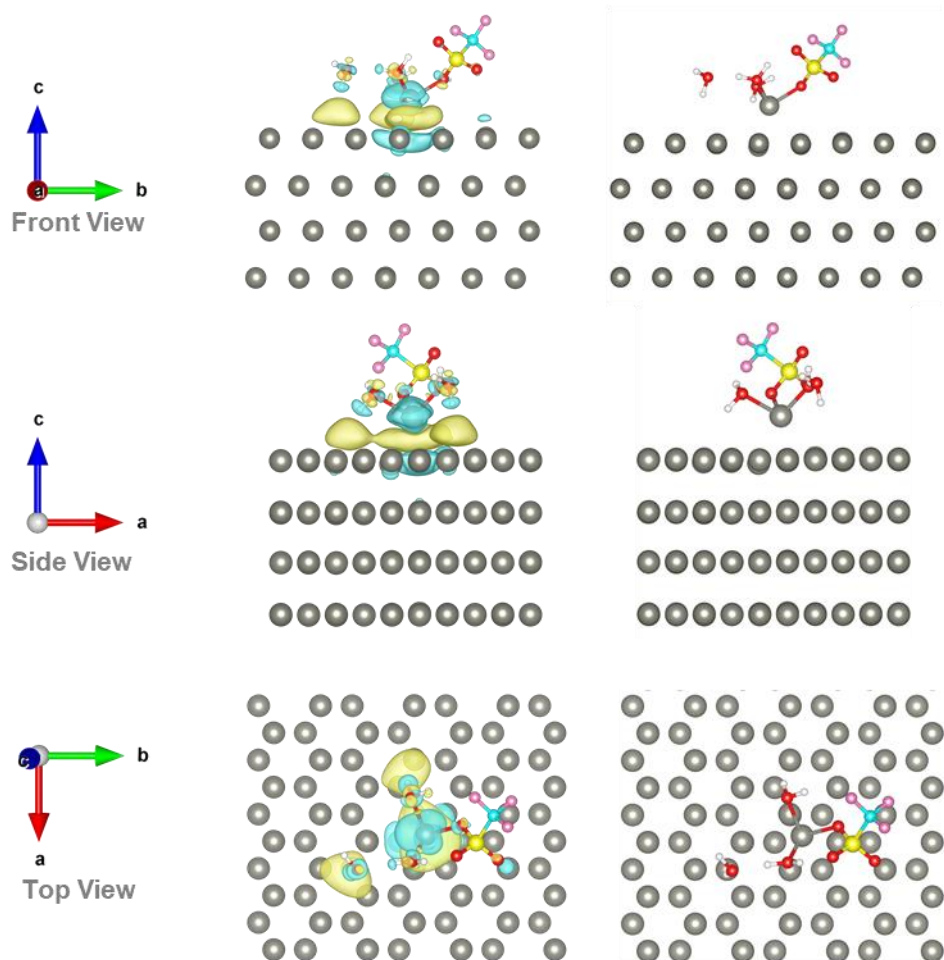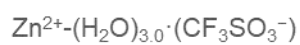
Zn^{2+}-$(H_2O)_{3.0}$·$(CF_3SO_3^-)$

Fig. S27. The charge density difference for demonstrating interfacial specific adsorption model of anode for $Zn^{2+}-(H_2O)_3\cdot(CF_3SO_3^-)$. (Cyan: charge depletion; yellow: charge accumulation; isovalue=0.001 e $Å^{-3}$). The isosurface charge density on the right is removed.
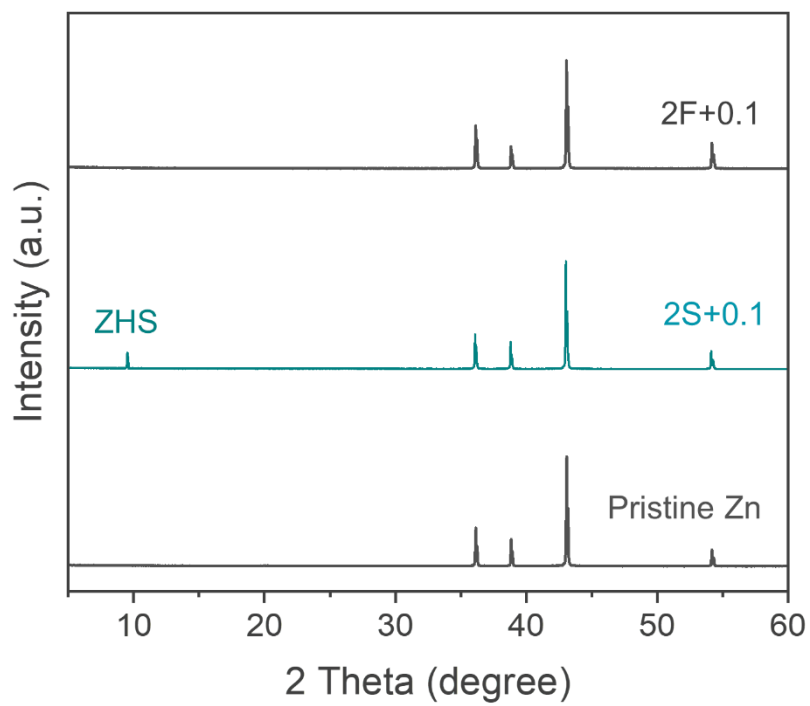
**Fig. S28.** XRD patterns of Zn anode after cycling in different electrolyte.
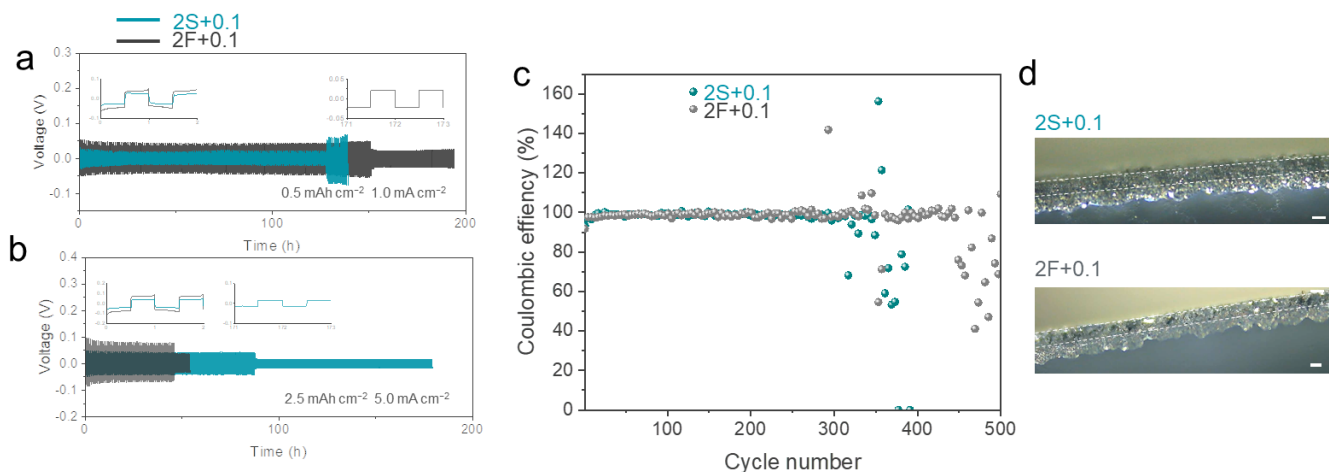
Fig. S29. Zn|Zn symmetrical cells with the different electrolytes to investigate the cycling performance with different area capacities and current densities of (a) 1 mAh cm^{-2} and 0.5 mA cm^{-2}, (b) 2.5 mAh cm^{-2} and 5 mA cm^{-2}. (c) Coulombic efficiency (CE) measurements of Zn/Ti cell with the different electrolytes. (c) *In-situ* optical microscopy visualization of Zn plating at 10 mA cm^{-2} for 30 min, scale bars: 30 μm.

The results show that the two electrolytes show low cycle stability and zinc dendrite characteristics.
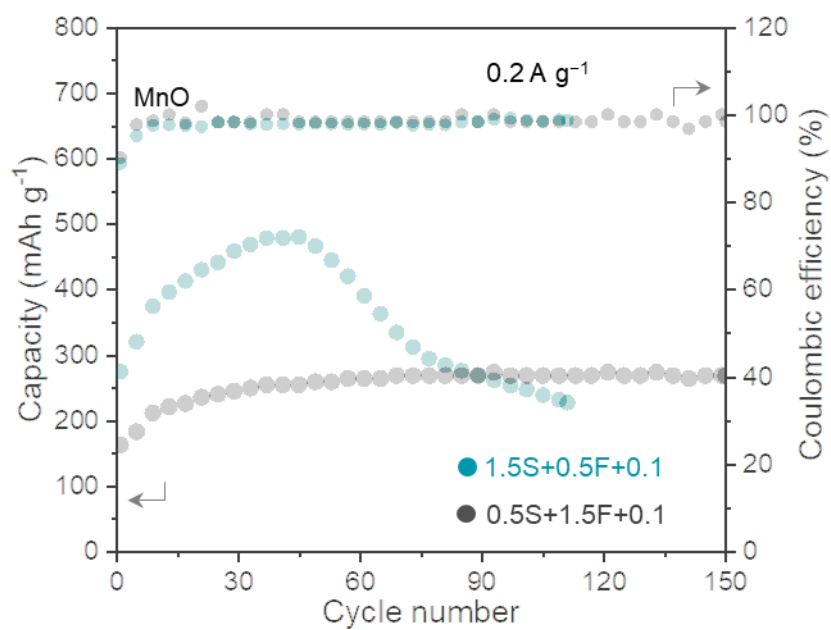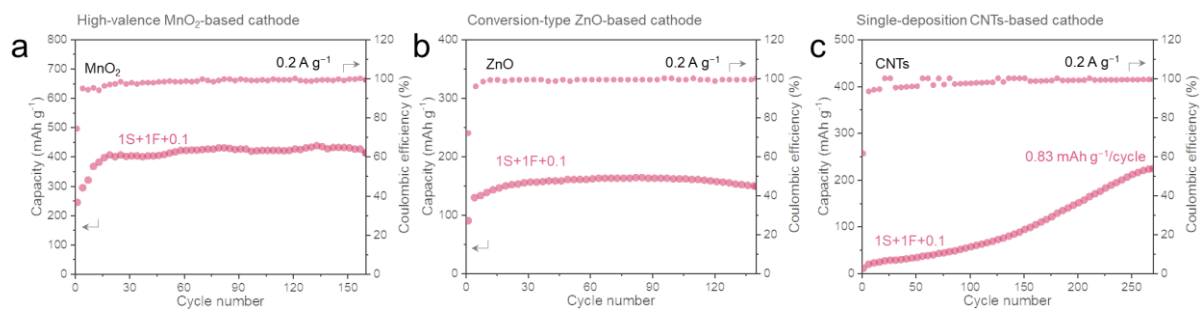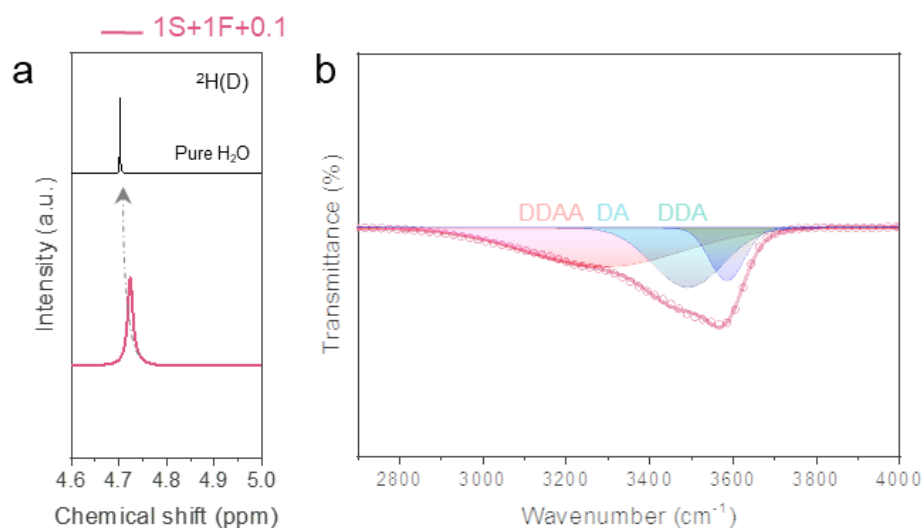
Fig. S30. Cyclic performance comparison of the cells in the different hybrid electrolytes using MnO-based cathode at 0.2 A g^{-1}.
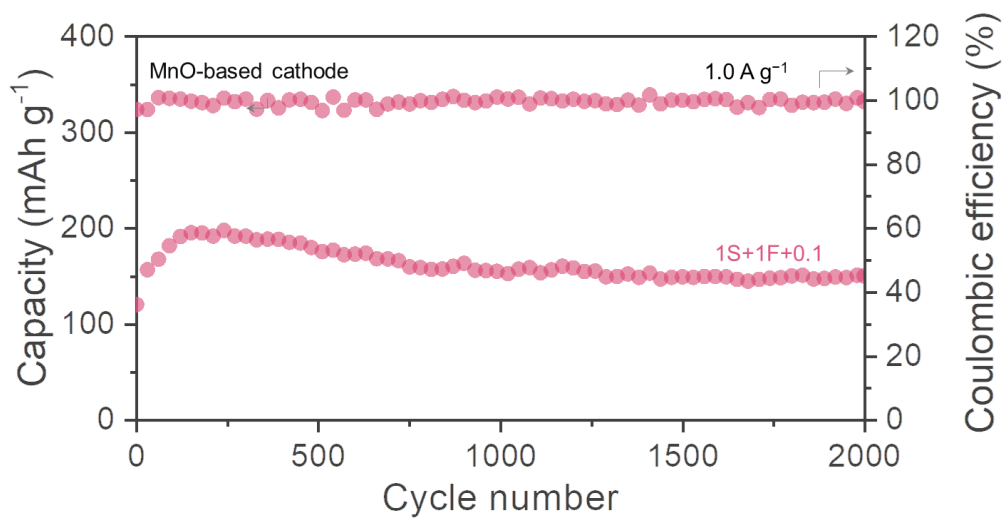
**Fig. S31.** Cyclic performance using MnO-based cathode at 1.0 A g^{-1}.

**Fig. S32.** Cyclic performance in the 1S+1F+0.1 electrolyte using MnO$_2$ (a), ZnO (b), and CNTs (c) cathode at 0.2 A g^{-1}.

Fig. S33. Investigation of 1S+1F+0.1 bulk electrolyte. (a) ^{2}H NMR spectra of H_2O. (b) The fitted FTIR spectra of water around $2700-4000$ cm^{-1}.The spectra of 1S+1F+0.1 electrolyte is disintegrated into five peaks with different donor (D) and acceptor (A), which are assigned to OH vibrations participated in DDAA (3239 cm^{-1}), DA (3428 cm^{-1}), and DDA (3565 cm^{-1}) hydrogen−bonding, respectively.
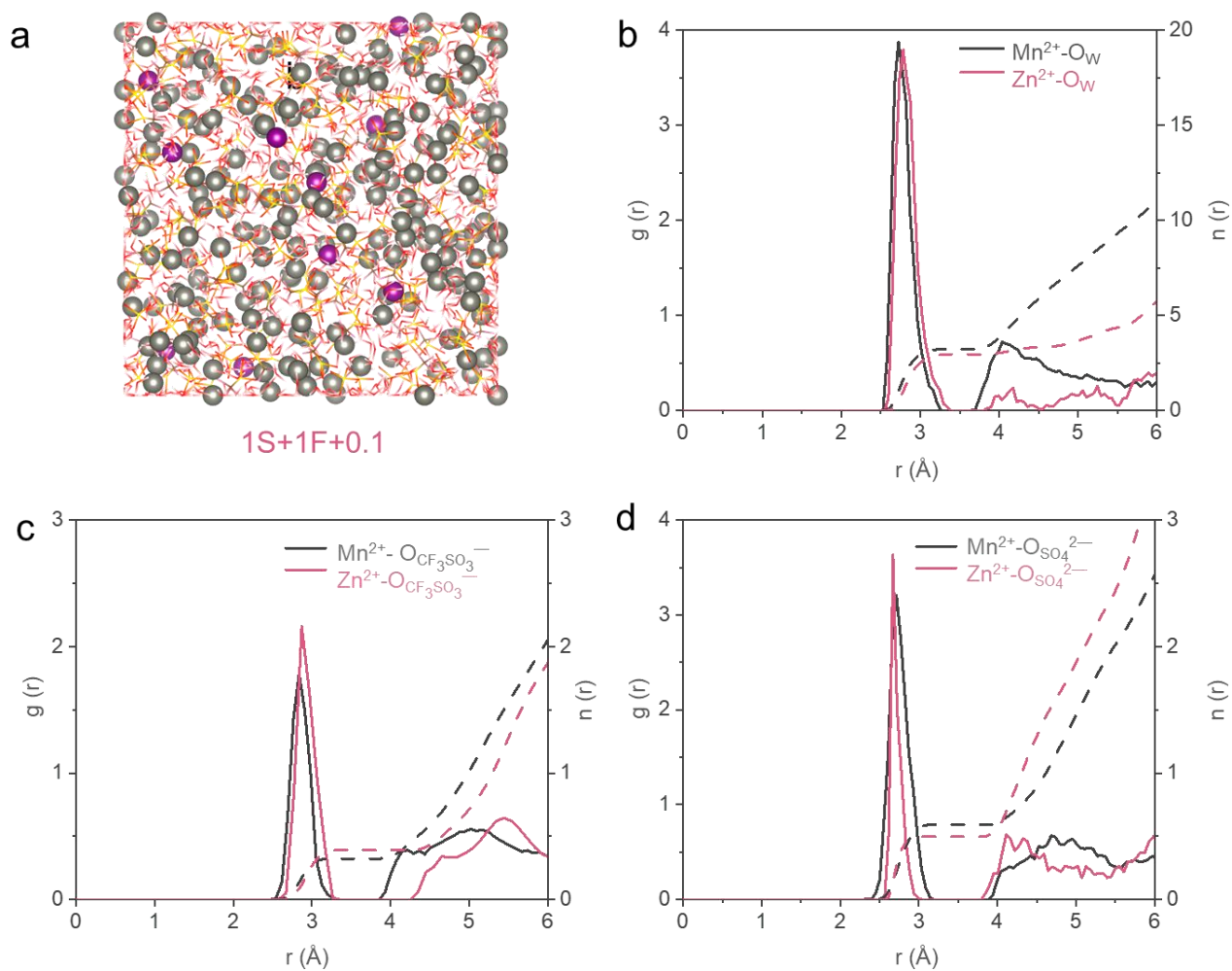
Fig. S34. (a) Snapshots of the equilibrated MD simulation box for 1S+1F+0.1 electrolyte. The cation solvation structures in 1S+1F+0.1 electrolyte is expressed based on the RDFs and coordination number analysis, respectively: (b) RDFs for Zn^{2+}/Mn^{2+}-O (H_2O), (c) Zn^{2+}/Mn^{2+}-O ($CF_3SO_3^-$), and (d) Zn^{2+}/Mn^{2+}-O (SO_4^{2-}).
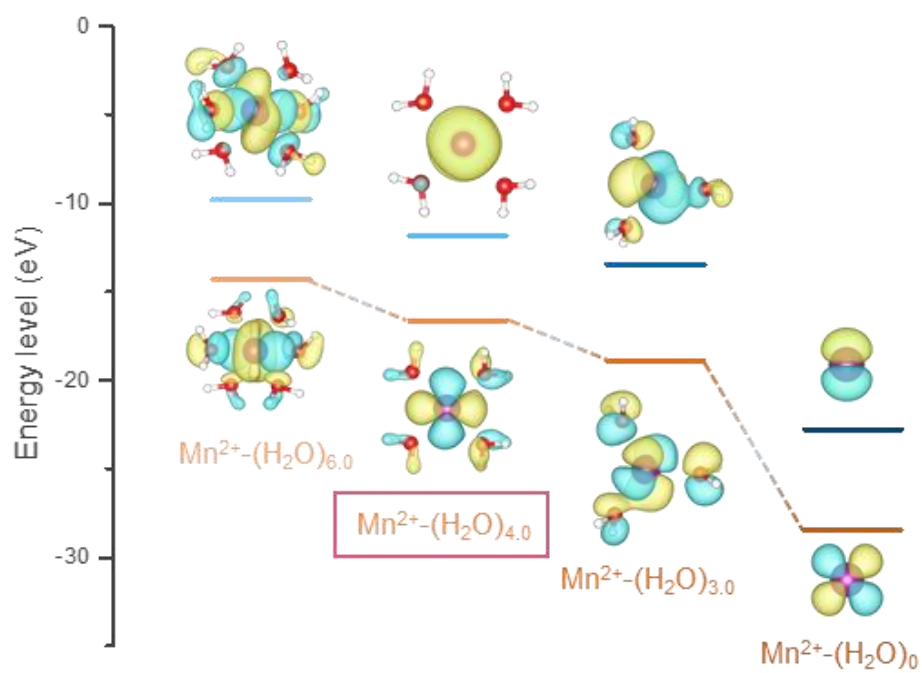
**Fig. S35.** HOMO/LUMO energy levels of Mn^{2+} combining with different number of H_2O.
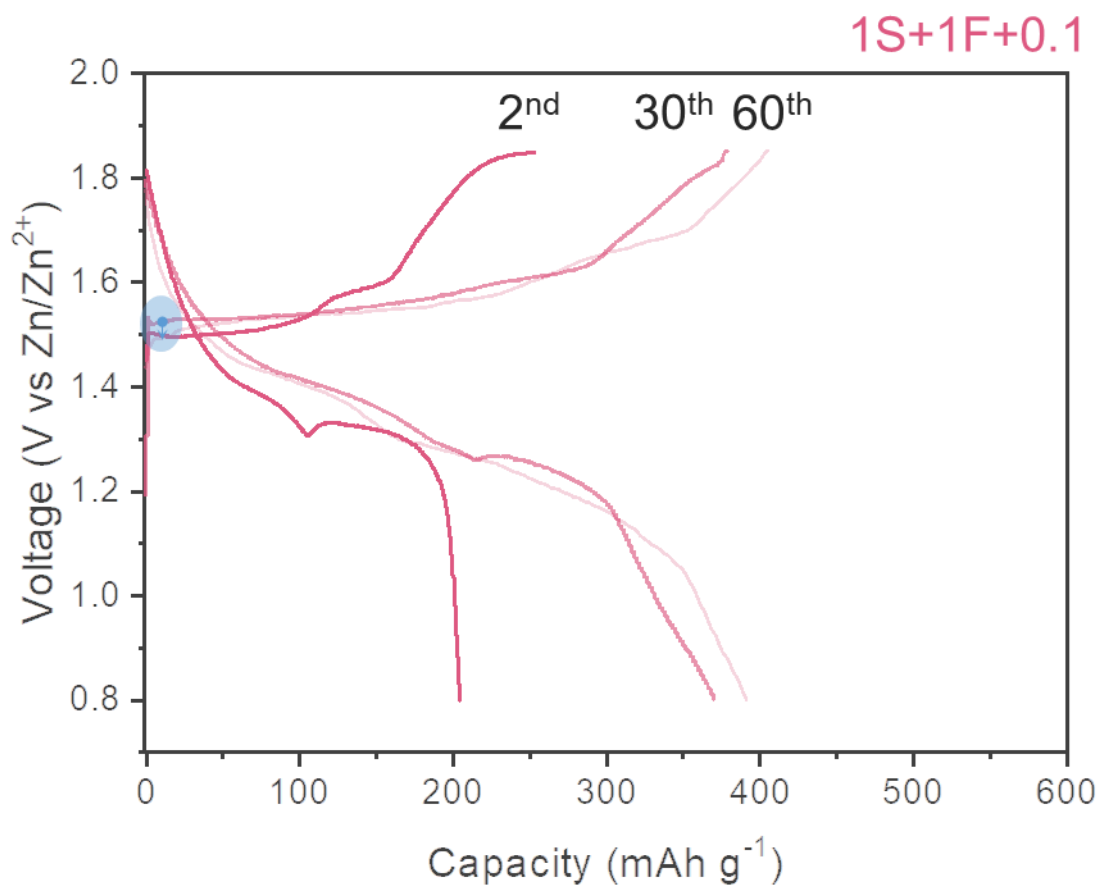
**Fig. S36.** Galvanostatic charge-discharge profiles of MnO-based cathode in 1S+1F+0.1 electrolyte.
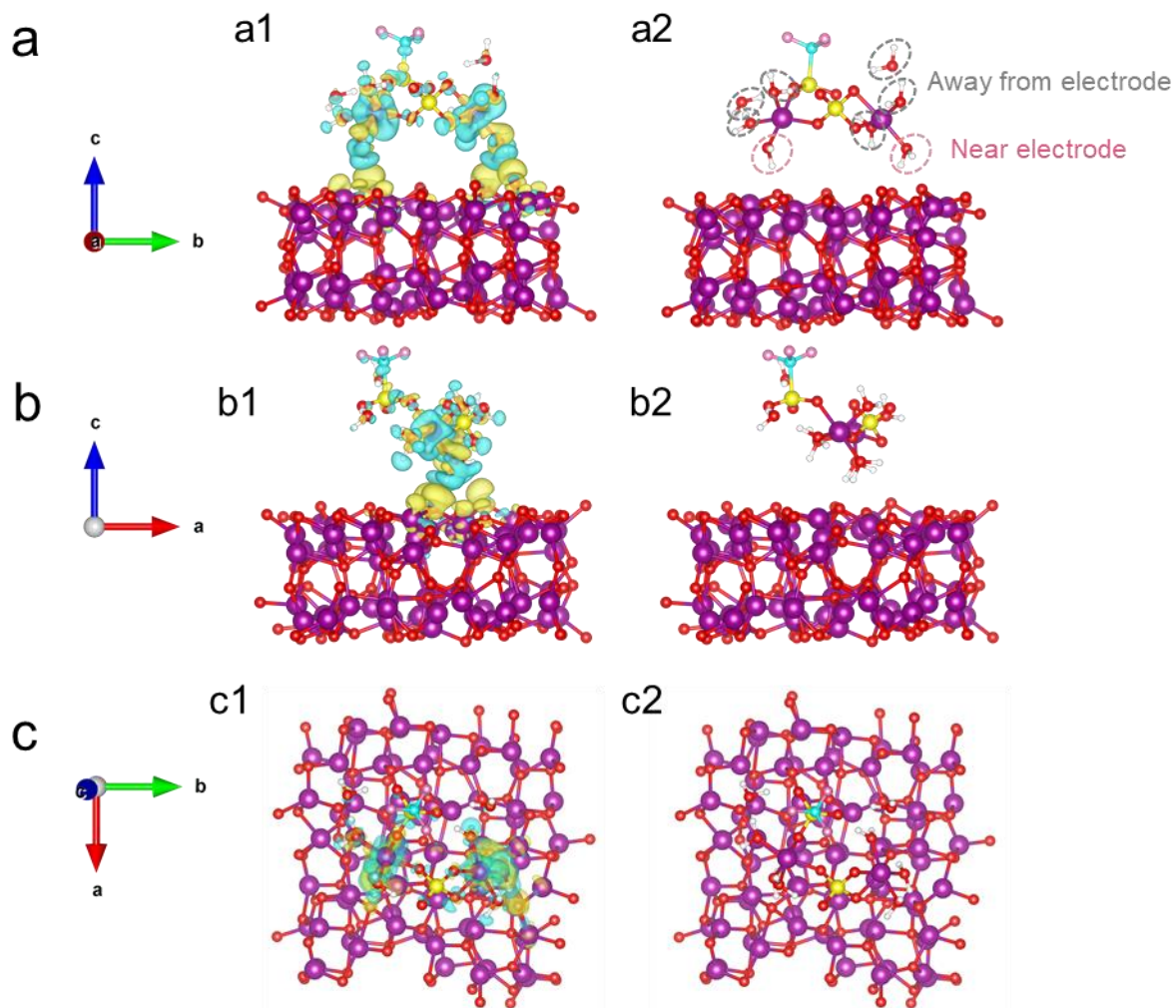
Fig. S37. (a1-c1) The charge density difference for demonstrating interfacial specific adsorption model of cathode for $Mn^{2+}-(H_2O)_4 \cdot (SO_4^{2-})_{0.5} \cdot (CF_3SO_3^-)_{0.5}$. (Cyan: charge depletion; yellow: charge accumulation; isovalue=0.001 e Å^{-3}). **(a2-c2)** The isosurface charge density is removed.
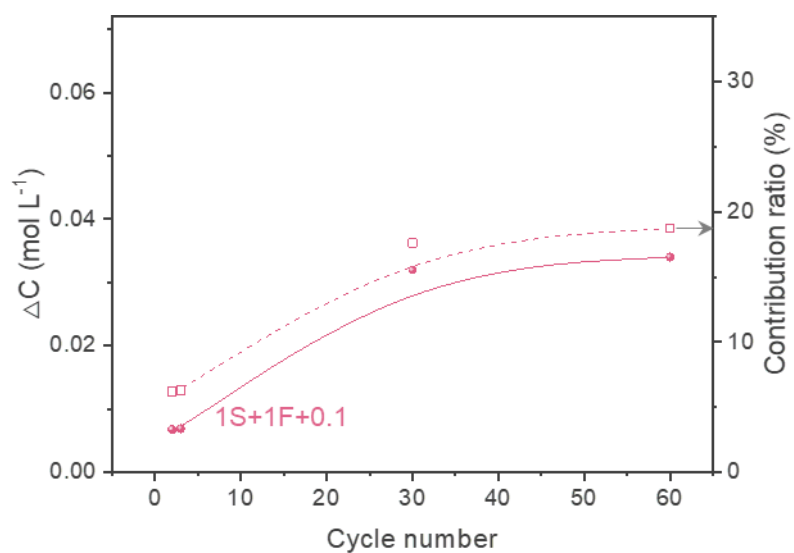
**Fig. S38.** Electrolyte behavior monitoring: the concentration changes (rectangle) and contribution ratios (ball) of the Mn^{2+} in 1S+1F+0.1 electrolyte.
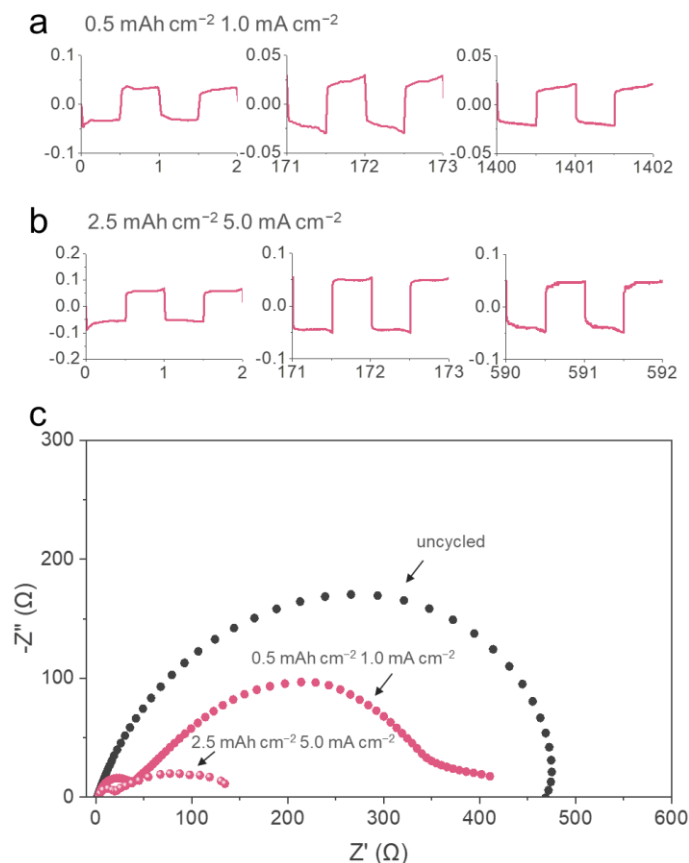
Fig. S39. (a-b) Local magnification of the symmetrical battery cycle curve of Fig. 5f-5g, respectively. (c) Impedance patterns of symmetric cells after cycling.

The polarization behavior of the voltage can be clearly observed from the local magnification (Fig. S39a-b). And as the current density increases, the impedance decreases to some extent and is not close to 0, indicating that there is no soft short circuit phenomenon (Fig. S39c).[11]
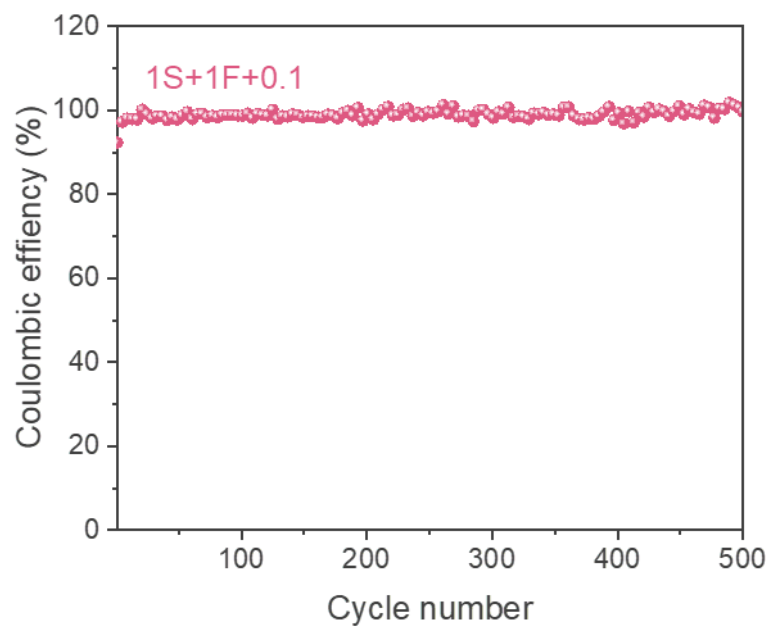
Fig. S40. Coulombic efficiency (CE) measurements of Zn/Ti cell with 1S+1F+0.1 electrolyte.
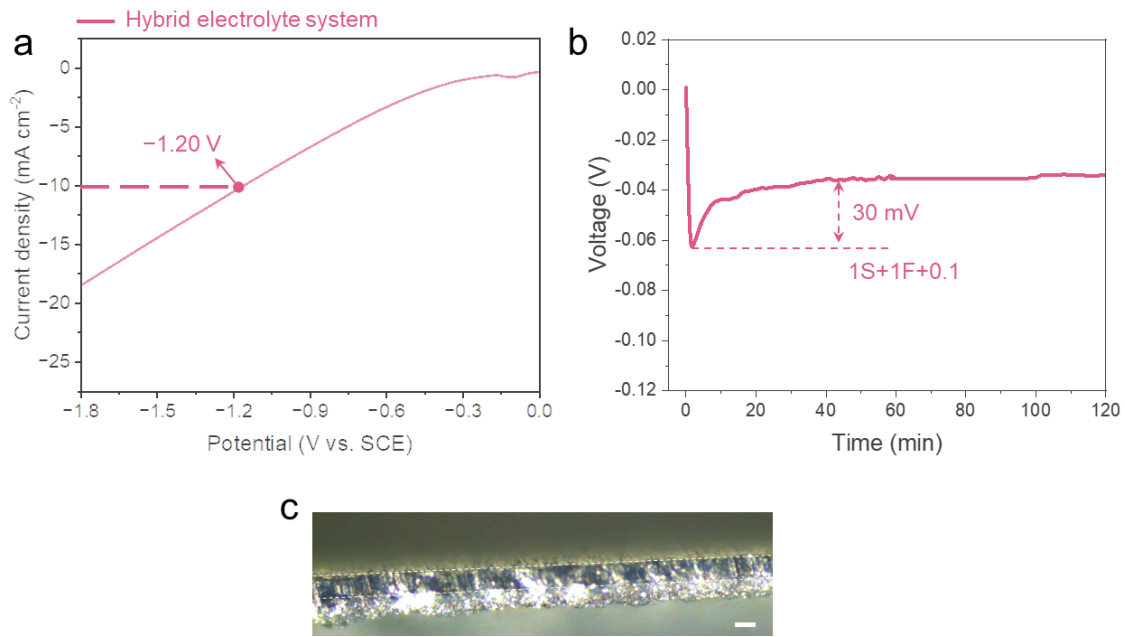
Fig. S41. (a) HER investigation in 1S+1F+0.1 electrolyte. Note that in order to avoid interference to HER by the Faradaic reaction of Zn^{2+}, the corresponding sodium salt was used as the test solute. (b) Initial Zn nucleation overpotential of Zn/Zn symmetric cells at 2 mA cm^{-2}. (c) *In-situ* optical microscopy visualization of Zn plating at 10 mA cm^{-2} for 30 min, scale bars: 30 μm.
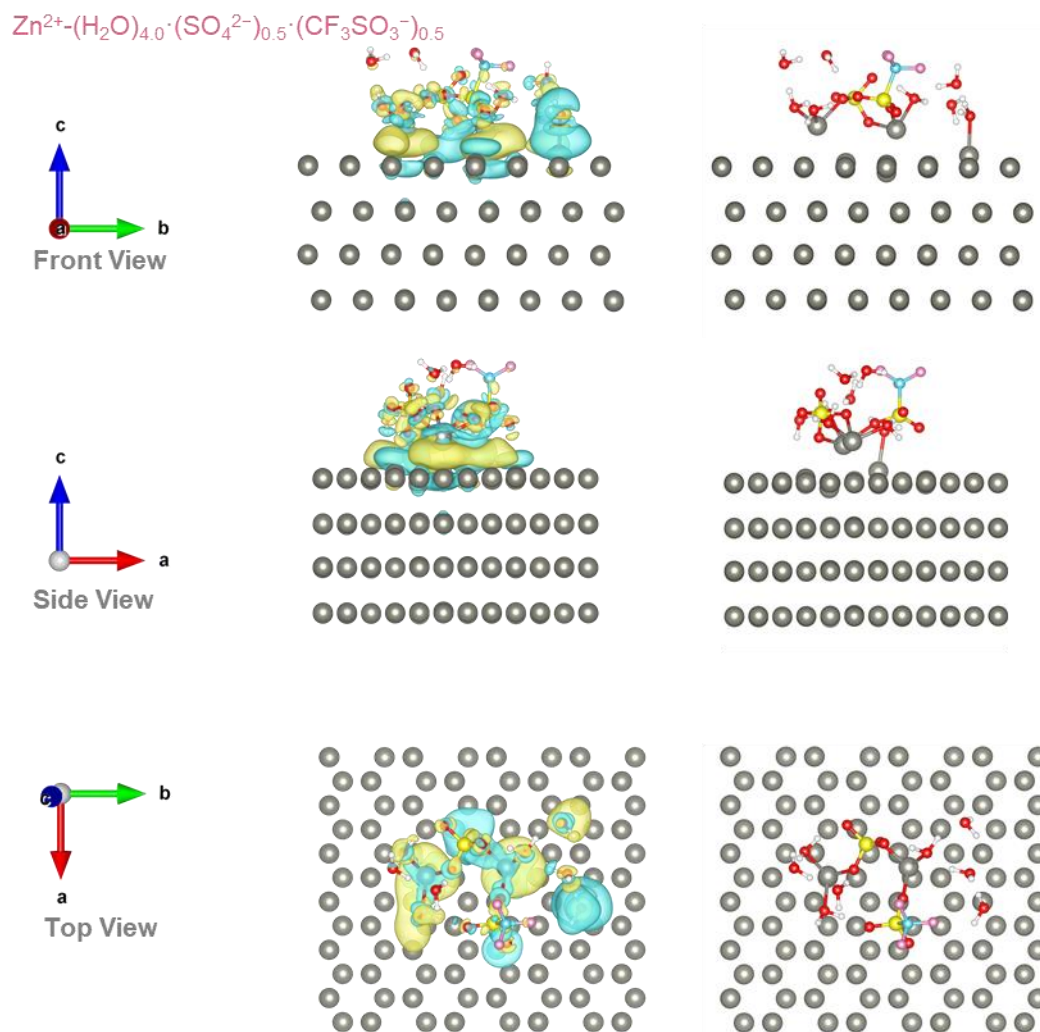
Fig. S42. The charge density difference for demonstrating interfacial specific adsorption model of anode for $Zn^{2+}-(H_2O)_4\cdot(SO_4^{2-})_{0.5}\cdot(CF_3SO_3^-)_{0.5}$. (Cyan: charge depletion; yellow: charge accumulation; isovalue=0.001 e $Å^{-3}$). The isosurface charge density on the right is removed.
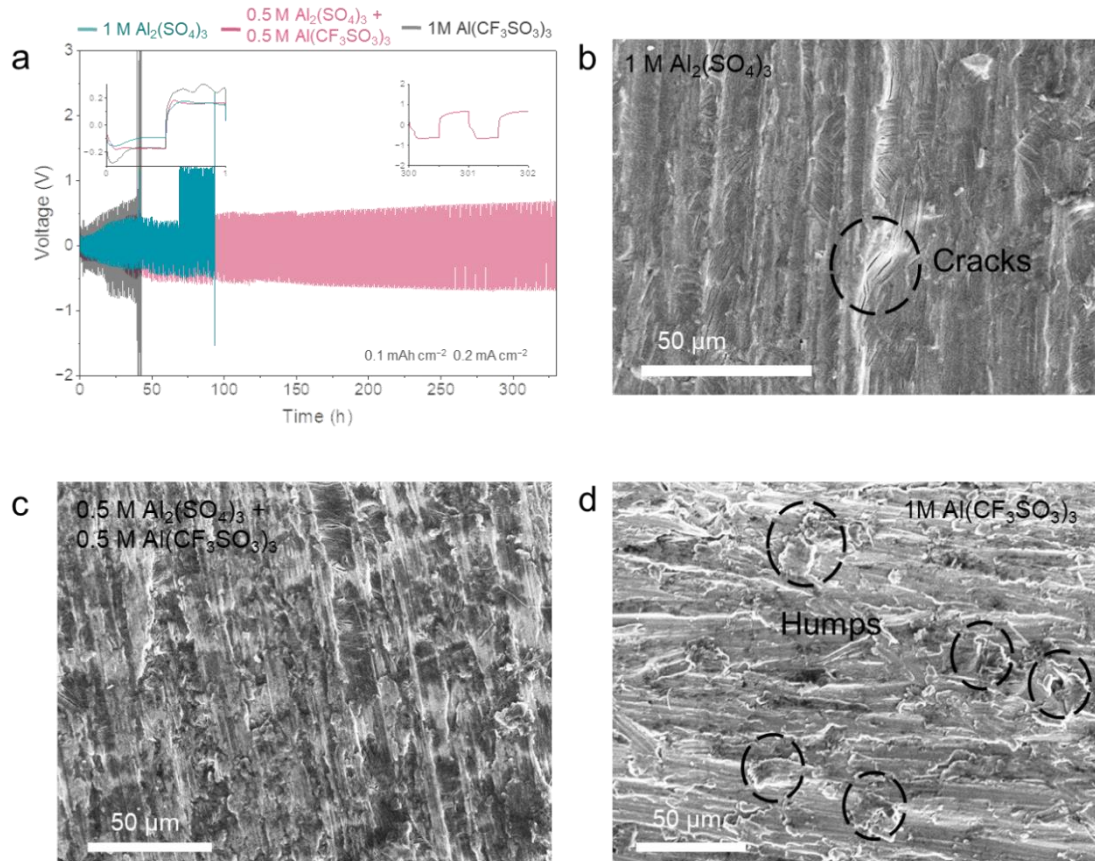
Fig. S43. Al|Al symmetric cells to investigate the cycling performance using different electrolyte with current density of 0.2 mA cm^{-2} and capacity of 0.1 mAh cm^{-2}. (b-d) SEM images of Al anode at a current density of 0.4 mA cm^{-2} and capacity of 0.2 mAh cm^{-2} under the different electrolytes obtained after 10 cycles.

References

1. C. Zhu, G. Fang, S. Liang, Z. Chen, Z. Wang, J. Ma, H. Wang, B. Tang, X. Zheng and J. Zhou, *Energy Storage Mater.*, 2020, **24**, 394-401.
2. W. Jiang, H. Shi, X. Xu, J. Shen, Z. Xu and R. Hu, *Energy Environ. Mater.*, 2020, **4**, 603-610.
3. Y. Liao, H.-C. Chen, C. Yang, R. Liu, Z. Peng, H. Cao and K. Wang, *Energy Storage Mater.*, 2022, **44**, 508-516.
4. H. Yang, W. Zhou, D. Chen, J. Liu, Z. Yuan, M. Lu, L. Shen, V. Shulga, W. Han and D. Chao, *Energy Environ. Sci.*, 2022, **15**, 1106-1118.
5. M. Zhou, Y. Chen, G. Fang and S. Liang, *Energy Storage Mater.*, 2022, **45**, 618-646.
6. X. Gao, H. Wu, W. Li, Y. Tian, Y. Zhang, H. Wu, L. Yang, G. Zou, H. Hou and X. Ji, *Small*, 2020, **16**, e1905842.
7. W. Li, X. Gao, Z. Chen, R. Guo, G. Zou, H. Hou, W. Deng, X. Ji and J. Zhao, *Chem. Eng. J.*, 2020, **402**, 125509.
8. Y. Guo, Z. Zhao, J. Zhang, Y. Liu, B. Hu, Y. Zhang, Y. Ge and H. Lu, *Electrochim. Acta*, 2022, **411**, 140045.
9. J. Hou, Y. Li, M. Mao, L. Ren and X. Zhao, *ACS Appl. Mater. Interfaces*, 2014, **6**, 14981-14987.

10.   W. Yang, Y. Zhu, F. You, L. Yan, Y. Ma, C. Lu, P. Gao, Q. Hao and W. Li, *Appl. Catal. B Environ.*, 2018, **233**, 184-193.
11.   Q. Li, A. Chen, D. Wang, Z. Pei and C. Zhi, *Joule*, 2022, **6**, 273-279.